Research Paper

GEOSPHERE

GEOSPHERE; v. 12, no. 2

doi:10.1130/GES01265.1

13 figures; 4 tables; 1 supplemental file

CORRESPONDENCE: jcoe@usgs.gov

CITATION: Coe, J.A., Baum, R.L., Allstadt, K.E., Kochevar, B.F., Jr., Schmitt, R.G., Morgan, M.L., White, J.L., Stratton, B.T., Hayashi, T.A., and Kean, J.W., 2016, Rock-avalanche dynamics revealed by large-scale field mapping and seismic signals at a highly mobile avalanche in the West Salt Creek valley, western Colorado: Geosphere, v. 12, no. 2, p. 607–631, doi:10.1130/GES01265.1.

Received 14 September 2015
Revision received 10 December 2015
Accepted 29 January 2016
Published online 29 February 2016

Rock-avalanche dynamics revealed by large-scale field mapping and seismic signals at a highly mobile avalanche in the West Salt Creek valley, western Colorado

Jeffrey A. Coe[1], Rex L. Baum[1], Kate E. Allstadt[1], Bernard F. Kochevar, Jr.[2], Robert G. Schmitt[1], Matthew L. Morgan[3], Jonathan L. White[3], Benjamin T. Stratton[4,*], Timothy A. Hayashi[2], and Jason W. Kean[1]

[1]U.S. Geological Survey, MS 966, Denver Federal Center, Denver, Colorado 80225, USA
[2]Mesa County Department of Public Works, 200 S. Spruce St., Grand Junction, Colorado 81502, USA
[3]Colorado Geological Survey, Colorado School of Mines, 1801 19th St., Golden, Colorado 80401, USA
[4]U.S. Forest Service, Gunnison District Office, 216 N. Colorado, Gunnison, Colorado 81230, USA

ABSTRACT

On 25 May 2014, a rain-on-snow–induced rock avalanche occurred in the West Salt Creek valley on the northern flank of Grand Mesa in western Colorado (United States). The avalanche mobilized from a preexisting rock slide in the Green River Formation and traveled 4.6 km down the confined valley, killing three people. The avalanche was rare for the contiguous United States because of its large size (54.5 Mm^3) and high mobility (height/length = 0.14). To understand the avalanche failure sequence, mechanisms, and mobility, we conducted a forensic analysis using large-scale (1:1000) structural mapping and seismic data. We used high-resolution, unmanned aircraft system imagery as a base for field mapping, and analyzed seismic data from 22 broadband stations (distances <656 km from the rock-slide source area) and one short-period network. We inverted broadband data to derive a time series of forces that the avalanche exerted on the earth and tracked these forces using curves in the avalanche path. Our results revealed that the rock avalanche was a cascade of landslide events, rather than a single massive failure. The sequence began with an early morning landslide/debris flow that started ~10 h before the main avalanche. The main avalanche lasted ~3.5 min and traveled at average velocities ranging from 15 to 36 m/s. For at least two hours after the avalanche ceased movement, a central, hummock-rich core continued to move slowly. Since 25 May 2014, numerous shallow landslides, rock slides, and rock falls have created new structures and modified avalanche topography. Mobility of the main avalanche and central core was likely enhanced by valley floor material that liquefied from undrained loading by the overriding avalanche. Although the base was likely at least partially liquefied, our mapping indicates that the overriding avalanche internally deformed predominantly by sliding along discrete shear surfaces in material that was nearly dry and had substantial frictional strength. These results indicate that the West Salt Creek avalanche, and probably other long-traveled avalanches, could be modeled as two layers: a thin, liquefied basal layer, and a thicker and stronger overriding layer.

INTRODUCTION

Rock and debris avalanches are extraordinary, gravity-driven agents of rapid landscape change that are extremely hazardous because they move large volumes of rock and debris at high velocities over long distances (e.g., Voight, 1978). Avalanches typically occur in extremely steep, remote areas that are difficult to access. Eyewitness observations of avalanches are rare, and when there are eyewitnesses, their views tend to be obscured by dust, clouds, or rain. Therefore, the dynamics and evolution of avalanches are rarely observed firsthand and the timing of avalanche events is rarely known.

The terms "rock avalanche" and "debris avalanche" have sometimes been used interchangeably because they both describe rapid, granular landslides from steep mountainous slopes. In this paper, we follow the terminology of Hungr et al. (2014, p. 180 and 186) and discern a rock avalanche as an "extremely rapid, massive, flow-like motion of fragmented rock from a large rock slide or rock fall," and debris avalanche as an "extremely rapid shallow flow of partially or fully saturated debris on a steep slope, without confinement in an established channel." Using these criteria, we classified the landslide described in this paper as a rock avalanche because it was a massive, flow-like landslide of fragmented rock that initiated from a rock slide and traveled down a well-established valley.

Questions often asked about rock avalanches, including the one described in this paper, are: (1) What were the conditions and sequence of events that allowed such a large zone of material to fail (apparently en masse) and travel so far?, and (2) How can we better identify other locations where they may happen in the future? There have been many mechanisms proposed to explain the high mobility of rock avalanches (see Hungr [2006] and Pudasaini

*Present address: Bureau of Land Management, Anchorage Field Office, Anchorage, Alaska 99507, USA

and Hutter [2007] for a review), but recently, there has been some convergence on the ideas that rock avalanches are highly mobile because of a reduction in dynamic granular friction by liquefaction and entrainment of basal materials (e.g., Sassa, 1988; Hungr and Evans, 2004), and/or increased pore pressures from the presence of interstitial water (e.g., Legros, 2002; Kelfoun and Druitt, 2005) or crushed rock (e.g., McSaveney and Davies, 2007). Extensive horst and graben structures (hummocks) preserved in many avalanche deposits support these interpretations because they form when relatively strong material moves and spreads on top of a relatively weak underlying layer (e.g., Paguican et al., 2014). Many researchers have noted that moving avalanches behave like a fluid (e.g., Heim, 1932; Hsü, 1975; McSaveney, 1978; Davies, 1982; Iverson and Denlinger, 2001; Hungr, 2006), and most numerical models developed to simulate rock avalanches (as well as other types of granular flows) are based on these observations.

Since the late 1970s, numerical models have made impressive progress in predicting avalanche speed and travel distance, knowledge of both of which is essential for properly evaluating avalanche hazards (e.g., Denlinger, 2014). Many of these models are based on the pioneering work of Savage (1979) and Savage and Hutter (1989). These models use shallow-flow models to simulate rock avalanches as variably fluidized masses by varying viscosities (e.g., Hungr, 1995; McDougall and Hungr, 2004) or by accounting for frictional grain interactions (e.g., Denlinger and Iverson, 2001; Iverson and Denlinger, 2001; Kelfoun and Druitt, 2005). Although these models are able to accurately predict the location and thickness of deposits, they do not fully account for dynamic and evolving changes in pore pressure and grain arrangements that can affect driving and resisting forces. These forces control the formation of internal structures (e.g., faults, folds, hummocks) during flow movement. Model results do not include structures or explicit sequencing of avalanche components. Some recent models account for dynamic mechanisms by incorporating granular fluctuation energy (Bartelt et al., 2012) or the physics of fluid-solid coupling (e.g., Kowalski and McElwaine, 2013; George and Iverson, 2014; Iverson and George, 2014). Although these models now exist, there are few detailed investigations of avalanches that provide field-based maps of internal structures and precise timing and velocity information that can be used as ground truth for continued model development, testing, and application.

Existing maps of structures within avalanche deposits are typically at a small scale (1:50,000 or smaller) and produced from remote sensing imagery (Shea and van Wyk de Vries, 2008). Structures shown by these maps suggest that many volcanic avalanches move with a surging motion and internally deform (at least near the surface) along discrete shear surfaces. Iverson and Vallance (2001) pointed out that rock avalanches should have complicated time-dependent and spatially variable mechanical behavior that is dependent on flow depth, grain concentration, and pore-fluid pressure. Given this reasoning, one would expect that a complex pattern of structures would develop during the emplacement of an avalanche deposit. Large-scale (1:12,000 or larger), field-based maps of avalanche deposits and structures are rare, but such maps should help to constrain the timing and dynamics of avalanche motion, as well as the sequence of pre- and post-avalanche events. In the one example of large-scale (1:12,000) avalanche mapping of which we are aware, Glicken (1996) concentrated on mapping geologic units (rather than structures), and was able to constrain the sequence of events for the avalanche resulting from the massive rock slide–debris avalanche from Mount St. Helens (Washington, United States) in A.D. 1980.

Historically, the timing of avalanche event sequences, including accurate estimates of velocities, has been difficult to determine. However, over the last few decades (beginning with Berrocal et al. [1978] and Kanamori and Given [1982]), the application of seismic methods has begun to provide key avalanche detection and timing constraints. Seismic analysis of mass movements has become significantly more common over the past decade. This is likely because increasingly open data sharing and denser seismic network coverage have made it more common to serendipitously record avalanches on existing networks. One of the primary benefits of seismic analysis of mass movements is that seismic data are recorded during the event, while most other data are collected afterwards. Raw seismic data can provide precise timing (e.g., McSaveney and Downes, 2002) and even semi-automated detection (e.g., Helmstetter and Garambois, 2010; Yamada et al., 2012). For large and energetic events, seismic data can also sometimes be used to estimate source characteristics, namely the forces the mass movement exerted on the earth. This time series of forces, if correctly interpreted, can contribute significantly to our understanding of the event dynamics (e.g., Allstadt, 2013a; Ekstrom and Stark, 2013; Yamada et al., 2013; Hibert et al. 2014; Iverson et al., 2015). In some cases, basal friction and other parameters can even be estimated either directly from seismically derived products (e.g., Brodsky et al., 2003; Allstadt, 2013a; Yamada et al., 2013) or by using seismic analysis in conjunction with numerical landslide modeling (e.g., Favreau et al., 2010; Moretti et al., 2012, 2015).

Massive, energetic mass movements commonly radiate seismic energy in two distinct bands attributable to different scales of motion. Large-scale coherent accelerations like the mobilization, deceleration, and propagation over large features in the path generate long-period (low-frequency) seismic waves with periods of up to several tens of seconds, while the same event will also generate a separate band of high-frequency energy (~1 Hz and higher) attributable to more stochastic processes like individual impacts (Huang et al., 2007), frictional processes (Schneider et al., 2010), and increased agitation (Moretti et al., 2015). The high-frequency energy typically emerges gradually from the noise, commonly significantly later than the first long-period pulses from initiation. High-frequency energy is commonly highest during the propagation and deceleration, and can become elevated due to propagation over topography or bends in the path (e.g., Allstadt, 2013a; Hibert et al., 2014; Moretti et al., 2015).

In this paper, we use seismic data and a 1:1000-scale structural and geologic map to interpret the dynamics of a rock avalanche that occurred on 25 May 2014, in the West Salt Creek valley on the northern flank of Grand Mesa in western Colorado (United States) (Figs. 1 and 2). The rock avalanche mobilized from the downslope face of a rock-slide slump block and traveled

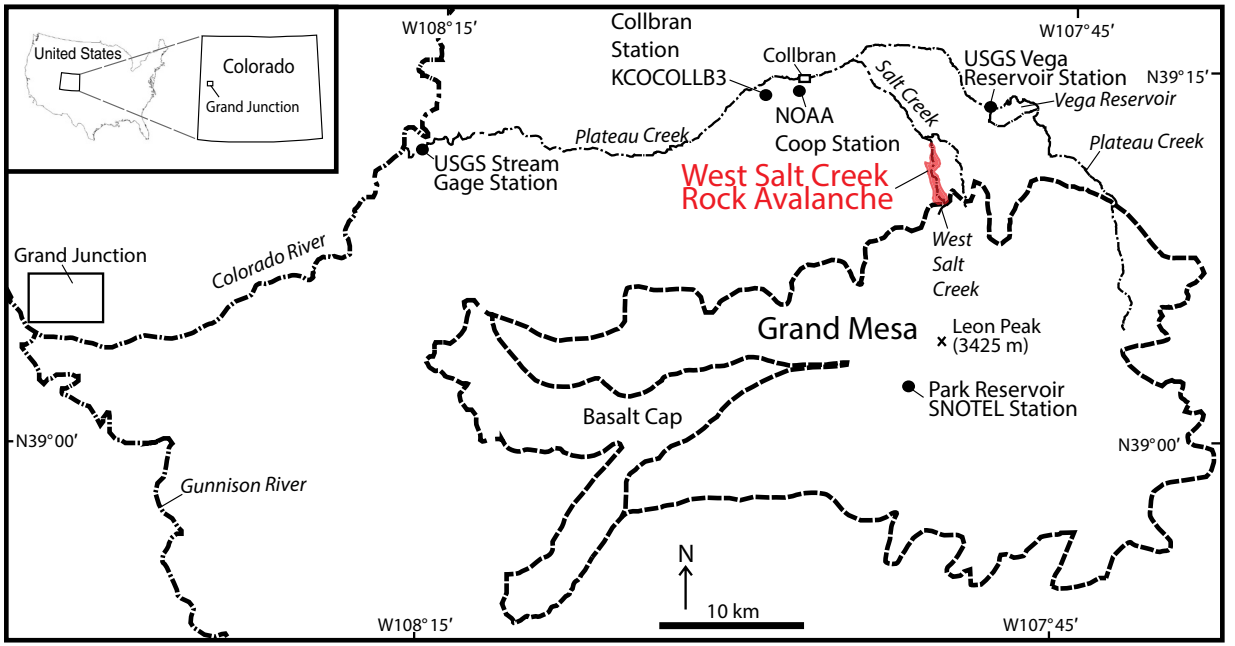

Figure 1. Map showing the location of the West Salt Creek rock avalanche. The rock avalanche covered an area of 2,448,988 m² (2.45 km²). The West Salt Creek drainage basin is 7.6 km², with ~2.0 km² located upslope from the head of the rock avalanche. USGS—U.S. Geological Survey; NOAA—National Oceanic and Atmospheric Administration.

~4.6 km down the confined drainage of West Salt Creek, killing three people working in the valley (White et al., 2015). According to the commonly used landslide mobility index *H*/*L*, where *H* is the maximum elevation traveled and *L* is the maximum length traveled, the avalanche was highly mobile with *H*/*L* = 0.14 (*L*/*H* = 7.2). For our detailed field mapping, we used a novel combination of high-resolution unmanned aircraft system (UAS) imagery and lidar data as base materials. We used our map, eyewitness accounts, and seismic signals recorded during the event to show that the rock avalanche consisted of a complex, cascading sequence of landslides that occurred throughout the day of 25 May. Our interpretation of these data focuses on (1) what can be inferred from the seismic signals and internal structures about the dynamics of highly mobile rock avalanches, and (2) how this new information improves our understanding of rock avalanche dynamics and can be used to constrain numerical models and hazard assessments.

GEOLOGICAL SETTING

Grand Mesa (Fig. 1) is a formerly glaciated upland in western Colorado that has a maximum elevation of ~3450 m, with 1400–1800 m of relief from the top of the mesa to surrounding river valleys. The mesa is underlain by Cretaceous and Tertiary sedimentary rocks and partially capped by Miocene basaltic lava flows (Yeend, 1969; Cole and Sexton, 1981; Ellis and Freeman, 1984; Kunk et al., 2002; Aslan, et al., 2010). Tertiary rocks underlie the basalt cap and form the northern flank of the mesa. These rocks consist of (from oldest to youngest) the Wasatch, Green River, and Uinta Formations, and the informally named Goodenough formation (Aslan et al, 2010; Cole, 2011). The Goodenough formation was previously known as an unnamed gravel and claystone unit (Yeend, 1969, 1973; Baum and Odum, 1996). The Wasatch, Green River, and Uinta Formations dip gently to the north, whereas the Goodenough formation is relatively flat lying.

Numerous Pleistocene and Holocene landslides lie along the flanks of Grand Mesa. In the western half of the mesa, most landslides are located on a "landslide bench" created by retrogressive rotational failures of basaltic caprock and subsequent transport of these basalt slump blocks by rotational and translational sliding in the Goodenough formation (Yeend, 1969, 1973; Baum and Odum, 1996, 2003). Some of these failures are probably ongoing, as Yeend (1973) documented movement rates of 4–15 cm/yr at the scarps of incipient basalt slump blocks.

In the eastern half of Grand Mesa where the West Salt Creek rock avalanche is located (Fig. 1), the basalt cap is absent, with the exception of a few remnants such as one underlying Leon Peak (Fig. 1; Aslan et al., 2010). The stratigraphy exposed by the West Salt Creek drainage consists of the Wasatch through Goodenough Formations (White et al., 2015), overlain by Pleistocene

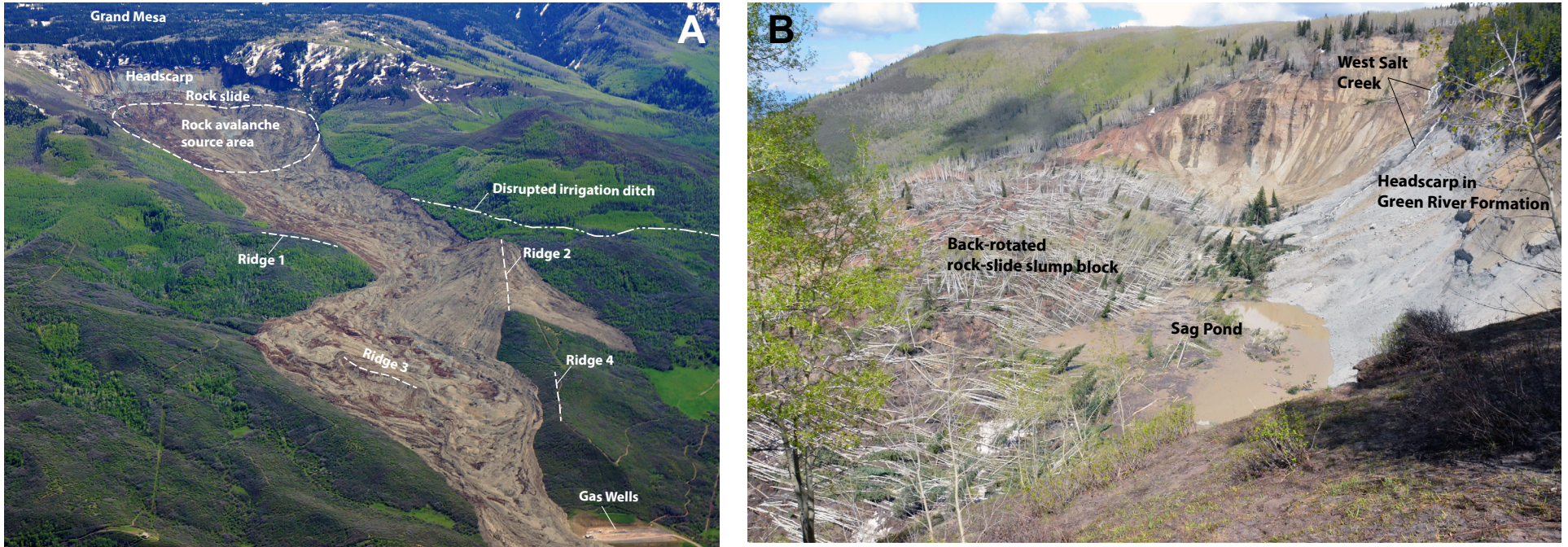

Figure 2. Photographs of the West Salt Creek rock avalanche. (A) View (to the south) of the avalanche in the West Salt Creek valley. Photo taken 27 May 2014. The curvilinear distance along the rock avalanche travel path from the top of the headscarp to the toe of the rock avalanche near the gas wells is 4.6 km. Photo courtesy of Mesa County Sheriff's Office. (B) Back-rotated rock-slide slump block and sag pond at the head of West Salt Creek. Photo taken 30 May 2014. The relief from the surface of the pond to the top of the active headscarp on the right is about 100 m. View is to the east.

glacial till on top of the mesa, and Pleistocene and Holocene colluvium on the flank of the mesa at the head of the drainage. A distinct red-colored, basalt-rich colluvium is located along the eastern side of the head of the drainage.

The rock avalanche originated from the reactivation of a preexisting rock slide (White et al., 2015) in the Parachute Creek Member (Bradley, 1931) of the Green River Formation (R. Cole, 2014, personal commun.). The Parachute Creek Member is the most economically important member of the Green River Formation because the dominant lithology is oil shale (e.g., Cole et al., 1995; Vanden Berg, 2008). However, at the head of West Salt Creek, the dominant lithologies are lean shales and marlstones. Previous landslide mapping on the north flank of Grand Mesa (Soule, 1988) identified the preexisting rock-slide deposit at the head of the West Salt Creek drainage, along with a wide range of other landslide types and ages originating from the Wasatch and Green River Formations, and multiple, long-traveled Pleistocene(?) basalt-rich debris flows that originated from Grand Mesa.

Data from interviews and aerial imagery indicate that the West Salt Creek valley bottom is typically very wet during spring snowmelt seasons. Interviews with members of the Hawkins family, who own the lower half of West Salt Creek valley, indicate that, prior to the rock avalanche, West Salt Creek was a perennial stream with peak flows in the spring. Google Earth imagery acquired in April 2012 shows at least a dozen ponds in the drainage, with one cluster in the upper half of the valley and one cluster in the lower half of the valley. Pre-avalanche, surficial geologic materials making up the valley floor were not mapped on small-scale geologic maps of the area, but we expect that the materials were a mixture of Quaternary alluvium, debris-flow and landslide deposits, colluvium, and possibly glacial till or outwash.

CLIMATIC SETTING AND METEOROLOGICAL CONDITIONS ON 25 MAY 2014

The Grand Mesa area has a continental climate with air temperature and precipitation correlated negatively and positively with elevation, respectively. For example, data collected between 1979 and 2014 at a SNOTEL (SNOwpack

TELemetry) station at Park Reservoir near the top of Grand Mesa (Fig. 1; Table 1) yield a mean annual temperature of 0.2 °C and mean annual precipitation of 1077 mm, whereas at a National Oceanic and Atmospheric Administration Cooperative Observer Program (COOP) station in the town of Collbran (Fig. 1; Table 1) on the north side of Grand Mesa (1161 m lower than Park Reservoir), data collected between 1900 and 1999 show a mean annual temperature of 7.9 °C and mean annual precipitation of 377 mm. At both stations, precipitation from November through March usually falls in the form of snow. On top of Grand Mesa, the maximum snow-water equivalent (SWE; the amount of water derived if snow on the ground were melted) usually occurs between 1 April and 15 May. May and June are relatively warm, so snow melts quickly and is completely gone by mid-May to 1 July.

An overview of the meteorological and hydrologic conditions in the area during the spring of 2014 are provided by the Park Reservoir SNOTEL station (snow depth and air temperature), a U.S. Geological Survey (USGS) station at Vega Reservoir (rainfall), a privately operated weather station near Collbran (station KCOCOLLB3; air temperature), and a USGS stream gage on Plateau Creek (streamflow; Fig. 1; Table 1). The elevations of the Park Reservoir and Vega Reservoir stations are closest (+176 m and –420 m, respectively; Table 1) to the elevation at the head of the rock avalanche (~2860 m; Table 1).

Records from the Park Reservoir and Plateau Creek stations indicate that snowpack, cumulative precipitation, and runoff in the spring of 2014, when the rock avalanche occurred, were all below historical averages. For example, at Park Reservoir, the maximum SWE during the spring of 2014 was 683 mm on 8 April, whereas the average annual maximum SWE for the 36 yr period of record at the station was 813 mm. Cumulative water-year precipitation (both snowfall and rainfall) through 25 May (i.e., the date of the rock avalanche) was 790 mm in 2014, whereas the long-term average was 846 mm. Peak discharge at the USGS stream gage was 50.7 m^3/s in the spring of 2014, whereas the average for the 79 yr period of record at the station was 51.6 m^3/s.

On 25 May, the snowmelt season was about three-quarters complete and snow depth was dropping rapidly (Fig. 3). Air temperature data indicate that the head of West Salt Creek was likely within the snowmelt-induced landslide season for the western United States identified by Chleborad (1998). Chleborad (1998) used landslide records to empirically define the snowmelt landslide season as the two-week period following the first occurrence of a 6 d moving average of daily maximum air temperature of 14.4 °C (58 °F). At Park Reservoir on the top of Grand Mesa, the 14.4 °C temperature threshold was exceeded on 1 June, ~6 d after the rock avalanche (Fig. 3). In Collbran, the snowmelt landslide season occurred in late March. Based on the elevations of the Park Reservoir and Collbran stations (Table 1), the 14.4 °C threshold was probably exceeded at the head of West Salt Creek during the week prior to 25 May.

The only unusual meteorological phenomenon during the spring of 2014 was rainfall on 25 May (Table 2; Fig. 3). This rainfall was unusual not because of total accumulation (~24 mm; Table 2) or intensity (~14.5 mm/hr; Table 2); it was unusual because it fell on snow, during the core of the spring snowmelt season on the north flank of Grand Mesa (including the head of West Salt Creek where the rock avalanche occurred). The rarity of this rain-on-snow event is difficult to assess given the lack of data available for the northern flank of Grand Mesa. However, McCabe et al. (2007) noted an increasing trend of rain-on-snow events in the southwestern United States at elevations above 2250 m, which includes the top and flanks of Grand Mesa.

METHODS

The methods that we used to reconstruct the movement dynamics and evolution of the rock avalanche consisted of three main elements: (1) gathering and analyzing eyewitness accounts from local residents; (2) field mapping and volumetric analysis of the rock avalanche; and (3) analyzing seismic

TABLE 1. METEOROLOGICAL STATIONS NEAR THE WEST SALT CREEK ROCK AVALANCHE

Station name	Elevation (m)	Elevation difference with respect to elevation* at headscarp of rock avalanche (m)	Distance from head of rock avalanche (km)	Period of record
SNOTEL station, Park Reservoir	3036	+176	14	1979–present
USGS station 09096100, Vega Reservoir	2440	–420	7	2007–present
NOAA COOP station 051741, Collbran	1875	–985	13	1900–1999
KCOCOLLB3, personal automated weather station near Collbran	1812	–1048	15	2013–present
USGS station 09105000, Plateau Creek	1475	–1385	36	1936–present

Note: See Figure 1 for locations. USGS—U.S. Geological Survey; NOAA—National Oceanic and Atmospheric Administration; COOP—Cooperative Observer Program.
*2860 m.

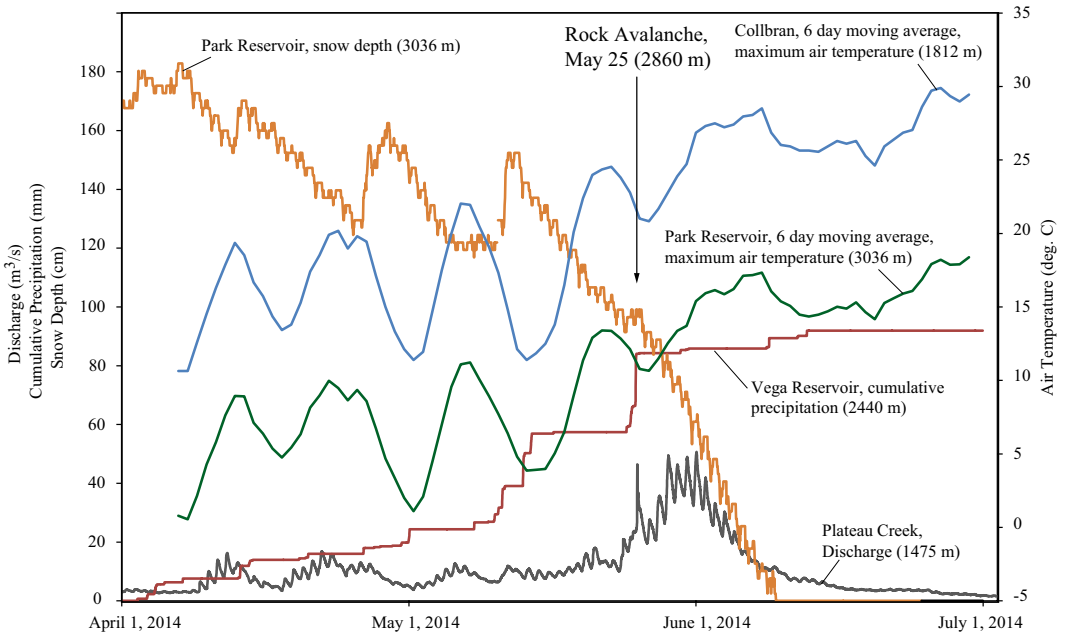

Figure 3. Diagram showing meteorological and hydrologic conditions near West Salt Creek in the spring of 2014. Elevations of the stations and of the head of the rock avalanche are indicated. Snow depth and streamflow discharge in the spring of 2014 were below historical averages. Rain-on-snow event on 25 May was unusual.

data that captured the event. For eyewitness accounts, we interviewed local residents while doing emergency response work in the two-week period immediately after the event, as well as during our mapping efforts later in the summer of 2014. We also reviewed accounts contained in two separate Mesa County Sheriff's Office reports of the incident. We used eyewitness accounts to complement our interpretations derived from field mapping and seismic data.

Field Mapping and Volumetric Analysis

Field work consisted of mapping rock avalanche structures, geologic units, and hydrologic features (springs, creeks, and ponds) in the field using orthorectified UAS imagery as a base map. All imagery was acquired using high-resolution Sony cameras in fixed-wing UASs between 26 May and 15 July 2014 (Table 3). All UAS takeoffs were by hand or catapult launch bungees, and

TABLE 2. RAINFALL RECORDED AT VEGA RESERVOIR ON 25 MAY 2014

Time period of rainfall	Duration (hr)	Rainfall amount (mm)	Estimated average recurrence interval* (yr)	Estimated annual exceedance probability* (%)	Estimated average recurrence interval† (yr)	Estimated annual exceedance probability† (%)
00:00 to 23:59	24	24.38	<1	>50	<1	>50
11:30 to 17:30	6	17.27	<1	>50	<1	>50
13:30 to 15:30	2	16.51	1	50	1–2	20–50
14:00 to 15:00	1	14.48	1–2	20–50	1–2	20–50
14:00 to 14:30	0.50 (30 min)	10.41	1	50	1–2	20–50
14:15 to 14:30	0.25 (15 min)	5.33	<1	>50	<1	>50

Note: Times shown are Mountain Daylight Times (MDT). Estimates of recurrence intervals and exceedance probabilities for peak rainfall of various durations are from the NOAA precipitation frequency atlas (Perica et al., 2013).
*At Vega Reservoir (39.2242°N, 107.8116°W).
†At rock avalanche headscarp in West Salt Creek (39.1647°N, 107.8472°W).

TABLE 3. SPECIFICATIONS FOR UNMANNED AIRCRAFT SYSTEM (UAS) FLIGHTS IN 2014

Date; launch time; duration of UAS flight	Type of UAS; cruising speed; pilot; number of flight observers	UAS camera	Nominal flying height (m); average ground sampling distance (m)	Area covered	Number of ground control points used	Number of photos acquired; percent photo overlap	Processing software; time required for processing	Products
26 May 2014; 16:30 MDT; 35 min	Falcon fixed wing; 51 km/hr; Chris Miser of Falcon Unmanned, Inc.; 2	Sony NEX7 24.3 megapixel	110; unknown	Lower third of the rock avalanche deposit	None, post-flight ground control was from photo-identifiable points	750; 75%	Photoscan; several hours	High-resolution orthophotograph mosaic; DEM
29 May 2014; ~15:00 MDT; 42 min	Trimble UX5 fixed wing; 80 km/hr; Frank Kochevar of Mesa County Public Works; 1	Sony 16.1 megapixel with custom 15 mm lens	75; 0.10	Headscarp, slump block, and upper third of the rock avalanche deposit	4, plus 4 photo-identifiable points	990; 70%	Trimble Business Center; several days	High-resolution orthophotograph mosaic; DEM; DSM
8 July 2014; ~12:00 MDT; 40 min	Trimble UX5 fixed wing; 80 km/hr; Frank Kochevar of Mesa County Public Works; 1	Sony 16.1 megapixel with custom 15 mm lens	250; 0.10	Middle third of rock avalanche deposit	7	990–1200; 60%	Trimble Business Center; 8–16 hours	High-resolution orthophotograph mosaic; DEM; DSM
11 July 2014; ~12:00 MDT; 40 min	Trimble UX5 fixed wing; 80 km/hr; Frank Kochevar of Mesa County Public Works; 1	Sony 16.1 megapixel with custom 15 mm lens	250; 0.10	Lower third of rock avalanche deposit	7	990–1200; 60%	Trimble Business Center; 8–16 hours	High-resolution orthophotograph mosaic; DEM; DSM
15 July 2014; ~12:00 MDT; 40 min	Trimble UX5 fixed wing; 80 km/hr; Frank Kochevar of Mesa County Public Works; 1	Sony 16.1 megapixel with custom 15 mm lens	150; 0.05	Upper third of rock avalanche deposit	7	990–1200; 60%	Trimble Business Center; 8–16 hours	High-resolution orthophotograph mosaic; DEM; DSM

Note: Imagery from July flights is shown in the Supplemental Figure (see text footnote 1). The structural, geologic, and hydrologic features (ponds, streams, springs) shown in the Supplemental Figure are as they existed in July 2014. MDT—Mountain Daylight Time; DEM—digital elevation model; DSM—digital surface model.

nominal flying heights ranged from 75 to 250 m, with average ground sampling distances between 5 and 10 cm. Between 1 June and 30 September 2014, we spent 10 person-weeks in the field mapping on this imagery at 1:1000 scale (e.g., Fig. 4). After field mapping, all map linework was transferred to a shaded-relief lidar base map derived from 1 m lidar data acquired by the Colorado Geological Survey during 1–3 June 2014.

For mapping of avalanche structures, we used terminology and classifications from structural geology. Previous work has shown that structures such as back-tilted surfaces, thrust faults, and normal and strike-slip faults are created by: (1) local variations in landslide speed, volume, and boundary geometry (Fleming and Johnson, 1989; Parise et al., 1997; Fleming et al., 1999; Parise, 2003; Coe et al., 2009; Guerriero et al., 2013, 2014; Handwerger et al., 2015); (2) variations in strengths of materials; and (3) driving and resisting elements within landslides (Baum and Fleming, 1991) indicated by normal faults (areas of extension) and thrust faults (areas of compression), respectively. We defined major surges in landslide movement using the mapped distribution of the structures within the avalanche deposit and rotated rock-slide block, as well as relations between geologic units. For example, strike-slip faults defined the lateral boundaries of a hummock-rich, central core of the avalanche that moved near the end of the failure sequence, whereas debris-flow deposits on top of this central core, but disconnected from their source area, indicated that the flows happened very early in the failure sequence.

Because the locations of hummocks are often important for interpreting mechanisms of avalanche movement (e.g., Paguican et al., 2014) and could potentially be used to interpret the emplacement velocity of paleolandslide deposits, we objectively mapped hummocks using 1 m contours of the post-event lidar data. Individual hummocks were identified from convex-upward bumps enclosed by 1 m contours. Where there were multiple closed contours at an individual hummock, the hummock was defined and mapped using the closed contour with the lowest elevation. This procedure was used for ~99% of hummocks. For the remaining 1%, we could not use this procedure because it was obvious that the closed contours with the lowest elevations defined pre-avalanche topography, that is, hills and ridgetops that existed before the avalanche occurred. In these locations, hummocks were mapped using the closed contours with the highest elevation.

We estimated the geometry and depth of the basal and lateral slip surfaces using two different methods, one for the back-rotated rock-slide block at the head of West Salt Creek, and one for the downslope avalanche deposit area. For the rock-slide block, we first constructed six two-dimensional profiles of the slip surface along five equally spaced transects in the direction of downslope movement and one transect perpendicular to the movement direction (Fig. 5). We drew these profiles by matching the ends of profile lines to areas where we knew that the slip surface intersected the ground surface. These areas included the headscarp, the lateral margins, and the downslope end of the rotated block where pre- and post-avalanche topographic data indicated that the avalanche deposit thickness was at or very near zero. We constrained the curvature of the profiles beneath the rock-slide block by making them flat-bottomed enough to account for observed back rotation of the block (Fig. 5) while still maintaining spiral shapes typical of landslide slip surfaces (e.g., Chen, 1975; Iverson et al., 2015). To create a three-dimensional slip surface, we used elevations along the profiles and the lateral boundaries of the block to interpolate a 1 m digital grid of the slip surface. To estimate the volume of the rock-slide block, we created

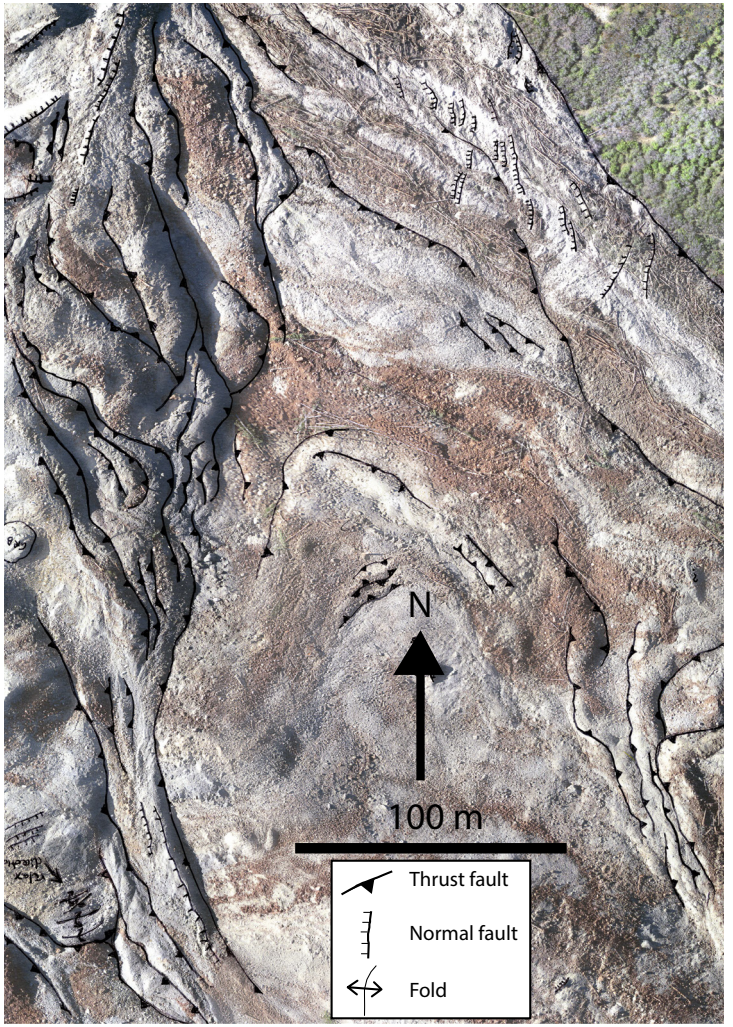

Figure 4. Example of an unmanned aircraft system image at West Salt Creek with structures from field mapping. See Figure 7 for location of image.

a difference grid by subtracting the slip-surface grid from the post-event lidar data, and summed all of the cell values in the difference grid. For the avalanche deposit area downslope from the rock-slide block, we created a separate difference grid by subtracting a pre-event USGS 10 m digital elevation model (DEM) from the post-event lidar data to determine the avalanche thickness. We estimated the volume of the deposit by summing all of the cell values in this difference grid.

We estimated errors for our volume estimates using two different methods, one for the back-tilted rock-slide block, and one for the avalanche deposit. For the rock-slide block, the primary volumetric error is associated with possible variations in the geometry and position of the slip surface. We calculated volumes based on our best estimate of the geometry and depth given available constraints, but other configurations and depths are possible. On the basis of these other slip surface configurations, we estimate that our rock slide volume could have an error of up to ±30%.

For the avalanche deposit, we estimated volumetric errors using an estimate of elevation error for the pre-event 10 m DEM data. Gesch et al. (2014) estimated that the overall root mean squared error (RMSE, equivalent to one standard deviation) for elevations in USGS 10 m DEM data for a mixed forest environment is 2.36 m. We consider the overall RMSE of post-event lidar data to be negligible in comparison. Therefore, we estimated volumetric errors using a two-standard-deviation value (4.72 m) and the number of 10 m DEM cells in the area of the avalanche deposit (16,072), using equation 5 of Coe et al. (1997).

Seismic Analysis

We analyzed seismic data from 22 distant broadband seismic stations (distances from the rock-slide source area ranged from 113 to 656 km; Fig. 6), operated by a number of different seismic networks (USArray Transportable Array [TA], United States National Seismic Network [US], University of Utah Regional Seismic Network [UU], Intermountain West Seismic Network [IW], Arizona Broadband Seismic Network [AE]), as well as data from a nearby short-period network (North Fork Valley Seismic Network [NF] run by the National Institute for Occupational Safety and Health). Though the short-period stations only record high frequencies (>~1 Hz) well, they are located significantly closer to the event (32–51 km) and thus contain valuable information that is attenuated before reaching the more distant broadband stations.

Beyond examining raw seismic data for event timing, we also inverted the broadband seismic data to estimate the force history, that is, the time series of forces that the landslide exerted on the earth, using the methods of Allstadt (2013a). This method exploits the theory pioneered by Kanamori and Given (1982) and supported by others (e.g., Eissler and Kanamori, 1987; Dahlen, 1993; Fukao, 1995) that the equivalent source mechanism of a landslide is a single force. This force is approximately equal but opposite in direction to the mass of the landslide times its acceleration. Accelerations include not only the mobilization and deceleration of the mass, but also centripetal accelerations as the mass moves through curves. In the latter case, the horizontal direction of the force points toward the outside of the curve because the acceleration is toward the center of the curve.

Seismic data used in the inversion were selected based on visual inspection for good signal-to-noise ratios and the lack of long-period noise after removing station response and converting from ground velocity to displacement. Noise is typically much stronger on horizontal components. Data selected included

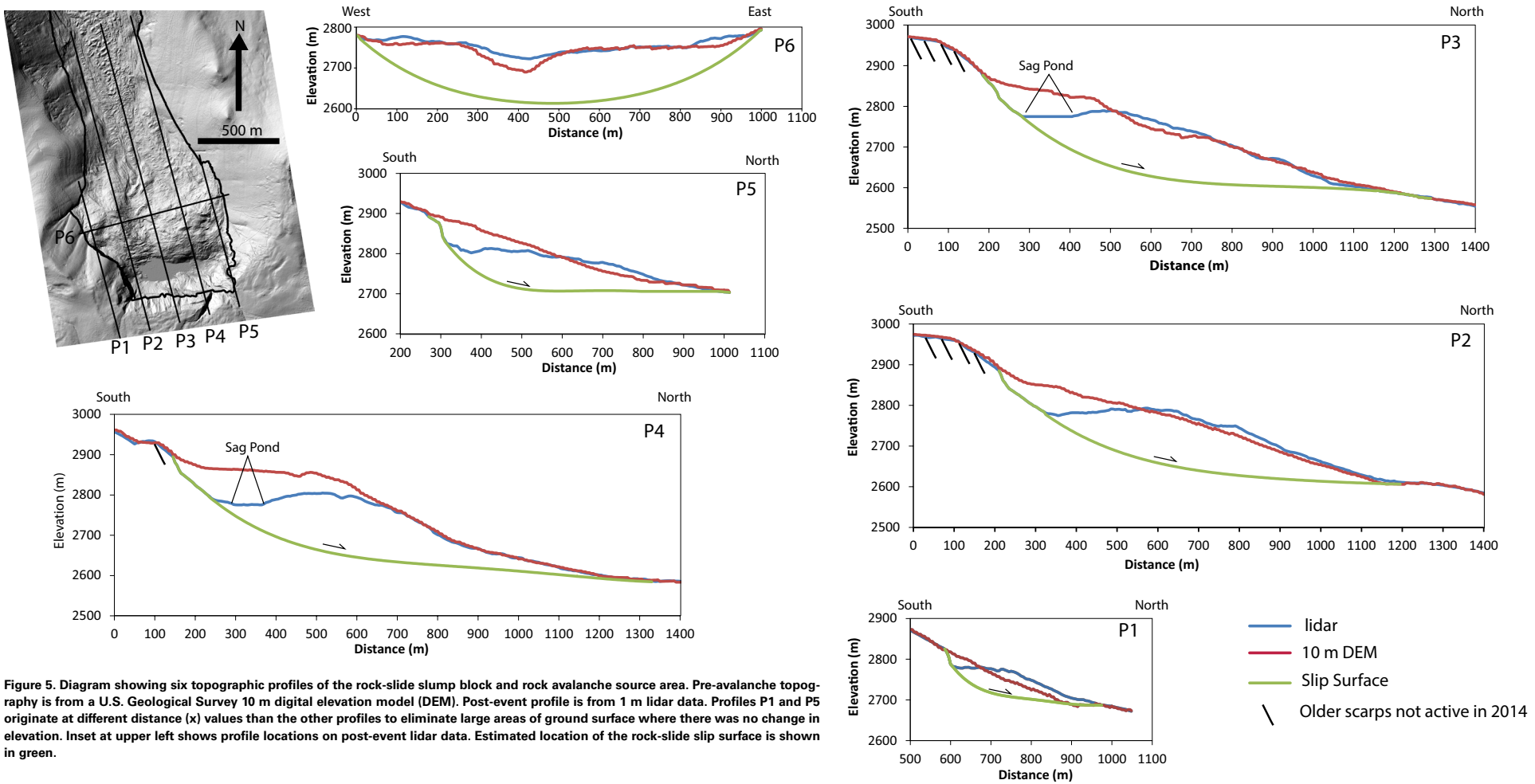

Figure 5. Diagram showing six topographic profiles of the rock-slide slump block and rock avalanche source area. Pre-avalanche topography is from a U.S. Geological Survey 10 m digital elevation model (DEM). Post-event profile is from 1 m lidar data. Profiles P1 and P5 originate at different distance (x) values than the other profiles to eliminate large areas of ground surface where there was no change in elevation. Inset at upper left shows profile locations on post-event lidar data. Estimated location of the rock-slide slip surface is shown in green.

22 vertical, eight transverse, and six radial channels. Ground displacement records were bandpass filtered with corners of 20 and 150 s. Identical filters were used on the Greens functions—the seismic waves that would be observed at each station for an impulse response at the source. Greens functions were computed using the Computer Programs in Seismology wavenumber integration method (Herrmann, 2002) with the ak135 velocity and attenuation model (Kennett et al., 1995). We used the inversion methods of Allstadt (2013a) to estimate the force history and methods described in Moretti et al. (2015), which are similar to the jackknife technique (Quenouille, 1956; Tukey, 1958), to estimate the uncertainties.

For a simple landslide, the force history can be used directly to approximate the trajectory if the mass is known and constant (e.g., Ekstrom and Stark, 2013; Hibert et al., 2014). However, in practice this simplification is complicated when there are events that overlap in time, when material elongates and flows rather than staying as a coherent block, and when the total moving mass changes over time due to multiple subevents or to entrainment and deposition (e.g., Allstadt, 2013a; Moretti et al., 2015). All of these factors are at play in this study, particularly because the majority of the mass remained in the source area, but we can still use the force history in conjunction with complementary information to gain significant insights into the event dynamics.

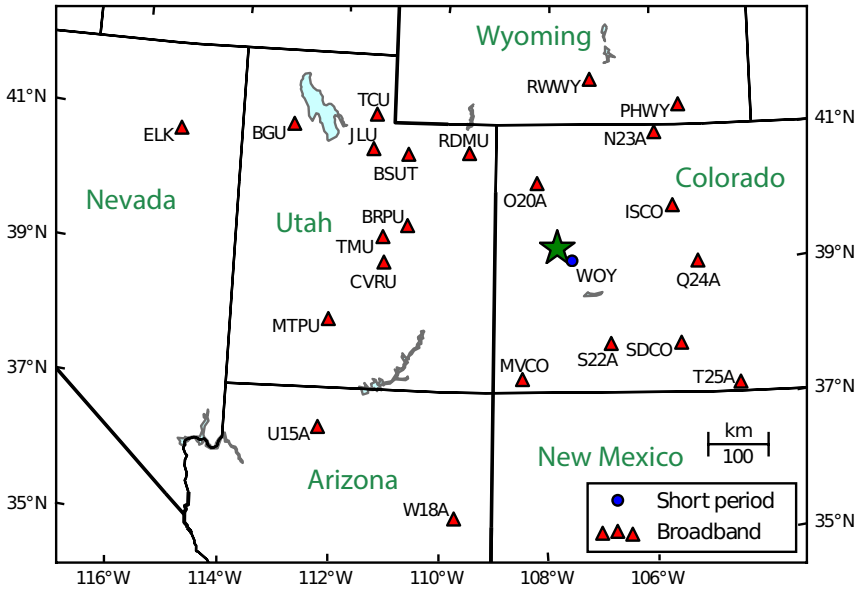

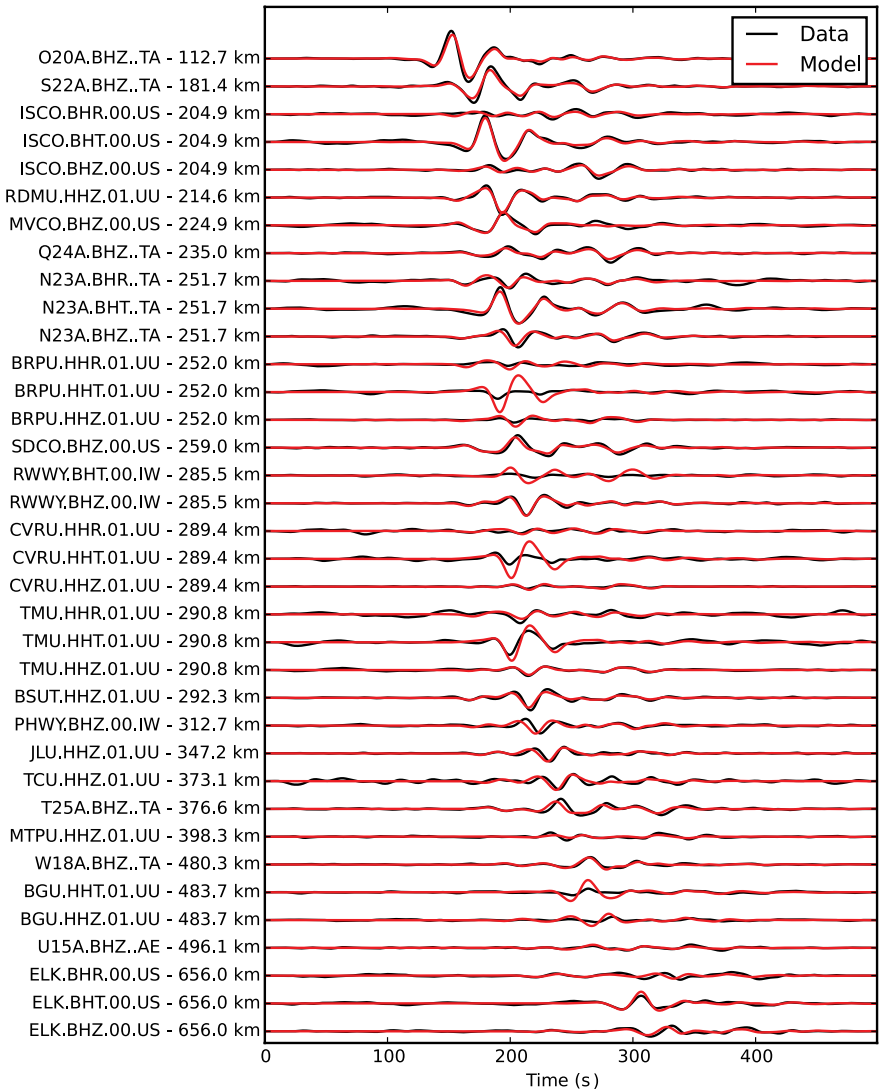

Figure 6. (Left) Map of seismic stations from which data were used in this study in relation to the West Salt Creek rock avalanche (green star). (Right) Broadband data used in seismic inversion. Black lines indicate data, which are displacement seismograms filtered between 20 and 150 s. Red lines show the data predicted from the seismically derived force history model (Fig. 13). The station labels indicate the station name, channel, location code (if applicable), seismic network, and the distance from the source area. When there is no location code, two sequential periods are shown in the station label. Time = 0 s corresponds with 23:41:40 UTC (17:41:40 local time).

The force history represents the spatial integral of forces being exerted on the earth at the source area at each point in time. Therefore, peaks in the force history should occur when the main portion of the moving mass reaches distinct geometric locations along the travel path that would generate strong accelerations, such as sharp curves. In order to exploit this deduction, however, we need to estimate the central flow path. A central path for the avalanche mass was chosen by comparing the fit of features of the force history to two potential paths: (1) the centerline of the depositional area, and (2) the valley bottom with a starting point at approximately the center of mass of the source area. We found that the path that best explained the features of the force history used the deposit centerline for the initial descent down the open valley, but then switched to the path that followed the valley bottom

once the avalanche became constrained by ridges. We assume uncertainties in the geographic locations tied to peak vectors of ±100 m for curve fits and ±25 m for the starting and stopping location of the center of mass of the rock-slide slump block.

In order to compare the timing of increased disruption and other smaller-scale processes that generate high frequencies to the large-scale motions represented by the force history, we adjusted the raw seismic data from a nearby short-period station, WOY.ELZ.NF (North Fork Valley Seismic Network), 31.7 km away, for travel times so the arrival times line up approximately with the force history. Due to the surface source, the wavefield is likely dominated by surface waves, so we used the Rayleigh group velocity for waves of period 1.0 s for western Colorado from Herrmann et al. (2013), which is 1.8 km/s, to estimate this time correction. To also simultaneously compare against the long-period displacement seismogram, we adjust the time of the displacement seismogram from the closest broadband station, O20A.BHZ.TA (Transportable Array), 112.5 km away, so that the first peak in displacement aligns with the first peak in the force history, which equates to a velocity of 2.6 km/s, similar to the group velocities reported by Herrmann et al. (2013) for periods of 10–30 s.

RESULTS

Eyewitness Accounts

Two reports by Mesa County sheriff's deputies (Fogg, 2014; Bridge, 2014) document eyewitness accounts of landslide movement on 25 May. Three primary accounts described landslide movement: (1) one from Melvin "Slug" Hawkins, the father of one of the three people killed in the landslide and whose house, which is located ~1 km northwest of the gas well pad shown in Figure 2A, has a view of most of the West Salt Creek drainage; (2) one from Tiffany and Melvin Bracco and their children, whose residence is east of the junction of West and East Salt Creeks; and (3) one from Eric Bruton, a member of the Plateau Valley Fire Department who searched around the lower third of the rock avalanche deposit for several hours immediately after it occurred.

The first indication that something unusual was happening in the West Salt Creek valley came from Slug Hawkins' account (Fogg, 2014). Between 0600 and 0700 h (local time) on 25 May he heard a "strange hissing noise" coming from the valley. Between 0930 and 1000 h, he looked out his window and noticed that "something didn't look right" on the flank of Grand Mesa at the head of West Salt Creek. About the same time, he heard from a neighboring rancher that the flow of water in an irrigation ditch originating in West Salt Creek (see Fig. 2A) had been disrupted. At this point, Mr. Hawkins drove to a ridge overlooking the West Salt Creek valley and noticed trees moving from slow ground movement along the east side of the head of the valley. Realizing that this movement was probably disrupting the irrigation ditch, he returned to his residence and called his son, Wes Hawkins, the water manager for the Collbran Conservancy Irrigation District. Between 1530 and 1630 h, Wes Hawkins, Clancy Nichols, and Danny Nichols entered the West Salt Creek valley to investigate the disruption of the irrigation ditch.

Between ~1730 and 1800 h, the Bracco family heard a loud rumbling sound that rattled the windows of their house (Fogg, 2014). They described the sound as "a low flying, large, military helicopter" (Tiffany), "a very long clap of thunder" (Melvin), and "a freight train coming" (children). From their residence, they did not have a view of the landslide area, so they did not immediately know the origin of the sound. About 10–30 min after hearing the sound, they got a call from Slug Hawkins saying that he had just noticed deposits indicating that a "massive slide" had occurred in the West Salt Creek valley. The Braccos responded by driving to Mr. Hawkins' residence, where Tiffany called 911 to report the landslide at 1817 h.

Eric Bruton was one of the first emergency responders to arrive at the landslide area. Between ~1830 and ~2030 h he conducted a search for Wes Hawkins and Clancy and Danny Nichols in the area around the landslide toe. During a 1 h period within this time window, he observed that a tree sticking out of the toe of the landslide deposit moved ~12 m (40 ft) downslope (Fogg, 2014; Bridge, 2014). Search operations continued the next day, 26 May, but were suspended at the end of the day due to ongoing concerns about slope instability. Search operations did not resume and the three people have not been found.

Field Mapping

Field observations during the last week of May 2014 (immediately after the event) indicated that the surface of the deposit from the 25 May landslide event was dry and that the event had two obvious components, a rock-slide block at the head of the drainage and a rock-avalanche deposit that originated from the northern downslope flank of the rock-slide block. The rock slide reactivated the preexisting rock-slide deposit at the head of the valley and formed a new headscarp at the base of the preexisting headscarp (Figs. 2 and 5). Lidar data revealed a network of older scarps upslope from the headscarp that were not activated during the May 2014 event (see Fig. 5 and White et al., 2015). The rock avalanche that mobilized from the rock slide rode up three ridges, spilled over two, and deposited material in the West Salt Creek drainage before terminating adjacent to a gas-well pad (Fig. 2A). The total curvilinear length (L) from the top of the newly formed headscarp to the downslope-most part of the deposit toe was 4590 m. The change in elevation (H) between the same two points was 636 m. The commonly used H/L and L/H mobility index values were 0.14 and 7.22, respectively, and the fahrböschung angle (defined as the inclination of the line connecting the top of the headscarp with the toe of the deposit) was 8°.

Our large-scale field mapping during the summer of 2014 revealed many details regarding landslide components and dynamics that were not obvious from preliminary field observations or from inspection of aerial photos and remotely sensed imagery. A 1:6000-scale version of our original 1:1000-scale map is shown in the Supplemental Figure[1]. A simplified version of the map is shown in Figure 7. Mapped structures and deposits show that the landslide

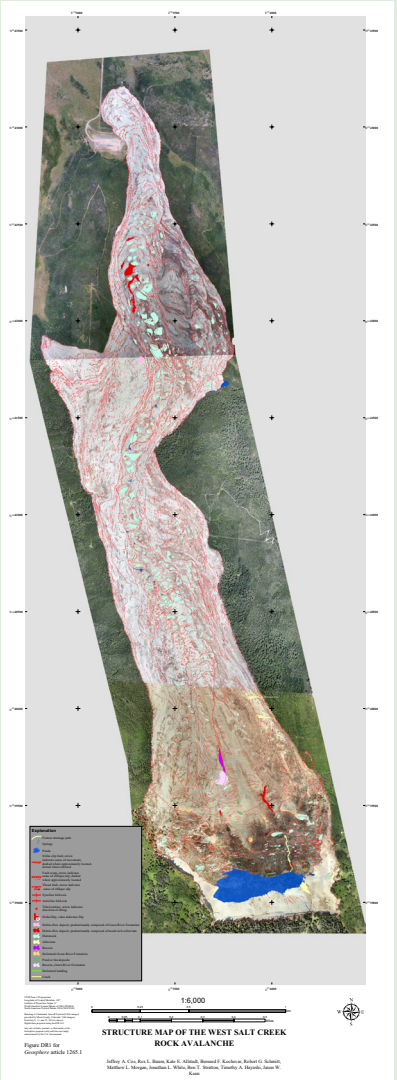

[1]Supplemental Figure. Structure map of the West Salt Creek rock avalanche. Please visit http://dx.doi.org/10.1130/GES01265.S1 or the full-text article on www.gsapubs.org to view the Supplemental Figure.

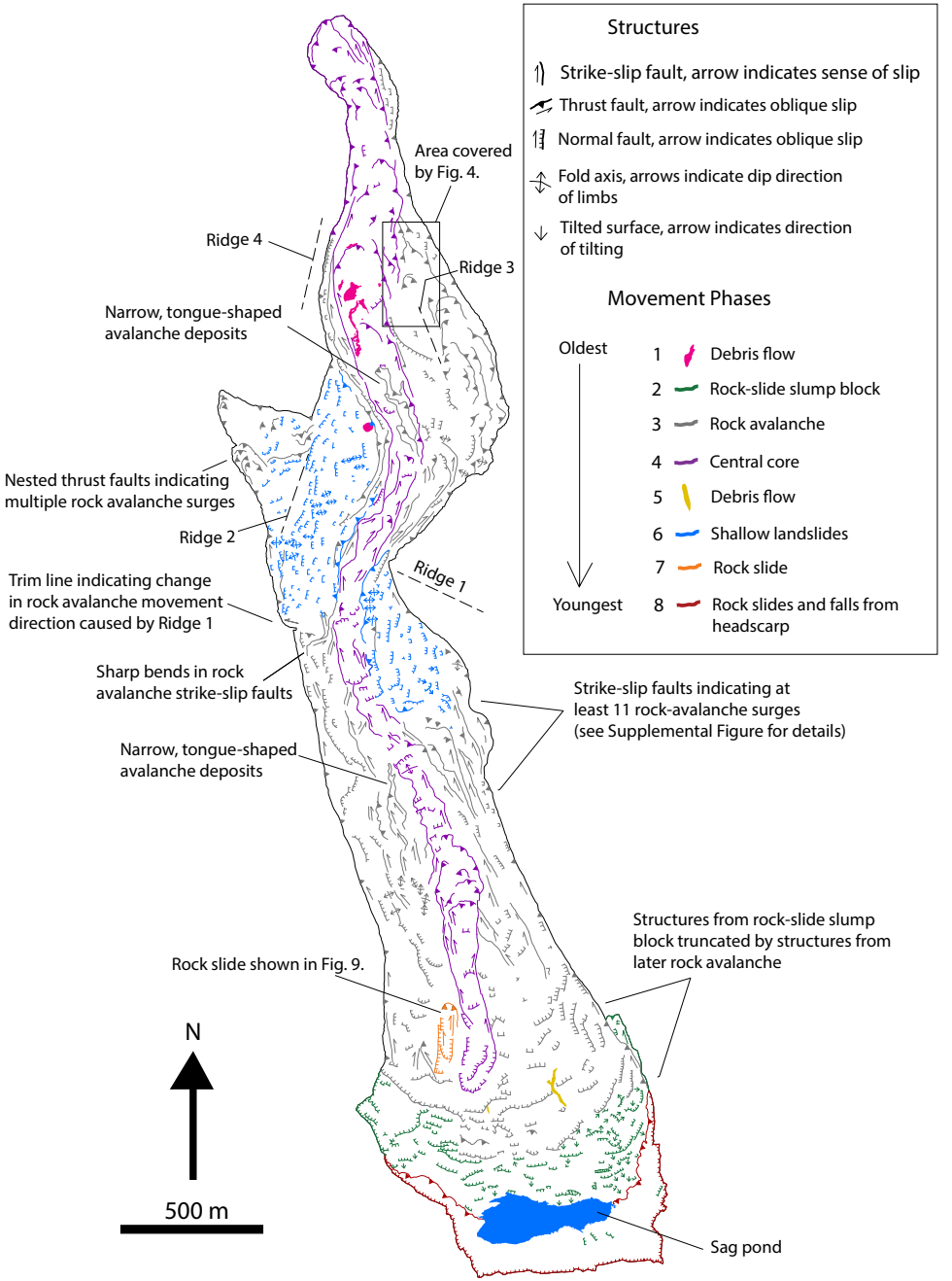

Figure 7. Simplified structural map. See the Supplemental Figure (see footnote 1) for a detailed map. Structures reveal eight major phases of movement, ranging from phase 1, which occurred ~10 h before the main rock avalanche (phase 3), to phase 8, which is ongoing (as of September 2015).

event was complex, with at least eight major phases. The eight phases (from oldest to youngest) were: (1) a landslide/debris flow; (2) reactivation, enlargement, and rotation of the preexisting rock-slide deposit; (3) the catastrophic rock avalanche; (4) movement of the central core of the rock avalanche, (5) a second debris flow, (6) failures of thin avalanche deposits on the steep flanks of the valley, (7) a rock slide on the steep, downslope face of the rock-slide slump block, and (8) rock slides and rock falls from the headscarp. Phases 1 through 5 happened on 25 May, and it is possible that there was some temporal overlap between these phases. Phase 6 was probably ongoing for at least several days after the event. Phase 7 occurred between 7 June and 18 August 2014, and phase 8 has been ongoing (as of September 2015) since 25 May. Below, we describe our map evidence for each phase.

Phase 1: Landslide/debris flow. The most direct evidence for phase 1 came from seismic data described in the Seismic Analysis section of this paper. However, the seismic data are consistent with (1) Slug Hawkins' description of hissing noises and slow movement on the downslope face of the preexisting rock slide deposit on the morning of 25 May, and (2) debris-flow deposits located on the lower third of the avalanche deposit (Fig. 7). The debris-flow deposits lie on top of avalanche deposits and are jumbled from traveling down the valley on the surface of the avalanche (Fig. 8A). There are red- and gray-colored deposits indicating that they had a source in both red basalt–rich colluvium and broken Green River Formation from within the preexisting rock-slide deposit, respectively. The most likely source for the debris flows was the steep downslope face described by Mr. Hawkins. Based on Mr. Hawkins' description, the debris flows were likely mobilized from a larger landslide failure on the face of the rock-slide deposit. However, the debris-flow deposits were the only depositional evidence for this larger failure that survived the later rock avalanche.

Phase 2: Rock slide. The fresh headscarp and the back-rotated and stretched slump block are the evidence for phase 2. Movement of the slump block is also obvious from topographic changes visible in pre- and post-event cross sections completed for volumetric analyses (Fig. 5). The newly created headscarp is ~100 m tall near the center of the rock-slide slump block (Figs. 2 and 5). Numerous normal faults and cracks related to north-south directed extension cut the surface of the slump block. These normal faults formed extensive horst and graben structures, including the fourth-largest horst (i.e., hummock, or in this case, a back-rotated block) in the valley (Fig. 8B). Overall back-rotation during movement ranged up to ~20°, which is the amount measured near the sag pond near the center of the block (Fig. 7). Local rotation of smaller blocks may have been >20°. Movement of the slump block resulted in a strike-slip fault and graben along the east side of the valley (Fig. 7). These structures are truncated by an oblique-slip (strike-slip and thrust) fault from movement of the catastrophic rock avalanche (phase 3, next section). These truncated structures, as well as continuous trim lines (i.e., deposits on the valley walls that mark the highest extent of the avalanche) extending from the lateral flanks of the block to the downslope deposit, indicate that movement of the slump block initiated the rock avalanche, not the other way around. The downslope and rotational motion of the rock slide provided the kinetic energy needed to mobilize the rock avalanche from the steep, downslope face of the block, which, because it was a preexisting rock-slide deposit, was already broken and loose.

Phase 3: Catastrophic rock avalanche. The obvious deposits along nearly the entire length of West Salt Creek and on adjacent ridges are the evidence for phase 3. Prominent flow bands of red, basalt-rich colluvium formed during movement of the rock avalanche (Fig. 8C). These bands are primarily in the eastern half of the deposit because the source of red colluvium is on the eastern side of the rock-slide slump block. The orientation of the long axis of flow bands in relation to movement direction is complex, with the long axis of some bands oriented in the direction of flow and others oblique or perpendicular to the direction of flow (Supplemental Figure; Fig. 8C). The elevations of trim lines along both sides of the upper, straight reach of the West Salt Creek valley indicate that the initial front of the avalanche was ~40 m above the thalweg of West Salt Creek. The avalanche initiated from the steep front of the slump block and left fault scarps where it broke away from the block. Flow bands of basalt-rich colluvium high on the east flank of the valley, and elongated in the downvalley direction, indicate that material was deposited along the edges and backside of the front as it passed. On the valley flanks, this material was generally <3 m thick. Following the passage of the front, cross-cutting relations of nested strike-slip faults along the east flank indicate that at least 11 internal movement stages (surges) occurred, with movement halting along the flanks first, and then progressively moving inboard toward the center of the valley (Fig. 7). Interestingly, some strike-slip faults on the western side of the valley had very high-angle (nearly 90°) bends in areas where there was no equivalent overall bend in the avalanche travel path (Fig. 7). To our knowledge, this characteristic has not been previously observed in strike-slip faults at slower-moving landslides (e.g., the Slumgullion earth flow in Colorado: Fleming et al., 1999; the Montaguto earth flow in southern Italy: Guerriero et al., 2013). Other structures associated with the avalanche included nearly exclusively normal faults in the source area on the face of the slump block, and normal faults and thrust faults in the middle portion of the avalanche deposit indicating that numerous episodes of both extension and compression occurred during the event.

Topographic ridges along the edges of the valley (Fig. 2) restricted the avalanche as it traveled downslope and caused changes in flow momentum that resulted in the avalanche changing direction. For example, at ridge 1 on the east flank, the direction in avalanche movement changed from north to a more northwesterly direction (Fig. 7 and 8C). This change in direction caused a drastic change in the trim line along the west flank, where the avalanche turned nearly 90° to the west, moved uphill (~20 m vertically), and spilled over ridge 2 (Fig. 7). Nested thrust faults on the west side of ridge 2 indicate that multiple surges overtopped the ridge. Most of the avalanche kept moving downvalley and rode over ridge 3 before turning back to the north and terminating near the gas well pad. Deposits on ridge 3 contain very few structures, probably because the deposit there is very thin.

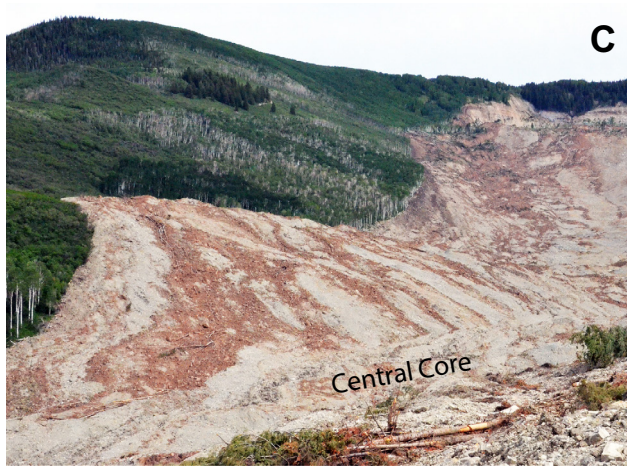

Figure 8. Photographs of mapped features. (A) Debris-flow deposit from movement phase 1. The visible part of the tree trunk in the foreground is about 3.5 m long. (B) Large hummock (2442 m² area, fourth largest in West Salt Creek) on the surface of the rock-slide slump block resulting from movement phase 2. The relief visible is about 15 m. (C) Red, basalt-rich flow bands (from movement phase 3) just south of ridge 1, which is located just outside the field of view to the left (see Fig. 2A for location). Flow bands show change in avalanche movement from a northward to a northwestward direction. Headscarp is visible at upper right. The length of the rock avalanche visible (from lower left to upper right) is about 2.5 km. (D) Strike-slip fault along the western edge of the central core. The diameter of the tree trunk in the foreground is about 20 cm. (E) Hummock in the central core. Large tree trunk visible in center of image is ~10 m long.

We did not observe any features (e.g., sand boils, mud splashes at the edges of the avalanche) that indicated liquefaction of valley material beneath the avalanche (not including the pre- and post-event debris-flow deposits). However, in many rock and debris avalanches, it is not unusual for direct evidence of basal liquefaction to be covered by rocks and debris (Hungr and Evans, 2004). Also, we did not observe any evidence for a dust cloud associated with the event.

Phase 4: Movement of the central core. Nested strike-slip (e.g., Fig. 8D) and thrust faults define a distinct central core that moved during phase 4 after the main avalanche had stopped (Fig. 7). At least part of the movement of this central core was witnessed by Eric Bruton during rescue operations on 25 May. As with the main avalanche, the central core contains a wide variety of structures. Strike-slip faults indicate at least five surges in movement of the central core, whereas thrust faults and thrust lobes indicate at least 10 surges in movement, although it is possible that some of these surges were occurring simultaneously. The head of the central core is at the steep, downhill face of the slump block, but the rest of the core is aligned with the pre-avalanche valley bottom. Hummocks dominate the topography of the central core (Fig. 8E).

Phase 5: Second debris flow. Debris-flow deposits high on the face of the slump block are the evidence for phase 5. These deposits are draped on normal faults that formed during the catastrophic rock avalanche.

Phase 6: Shallow landslides in rock-avalanche deposits. Normal faults that cut avalanche deposits (including flow bands) on moderate to steep (>~15°) flanks of the West Salt Creek valley are the evidence for phase 6 (Fig. 7). These steep slopes began failing after the central core stopped moving, and possibly continued to do so for at least several days. We know that the central core had stopped moving because some of the toes from the shallow landslides cover strike-slip faults along the edges of the central core.

Phase 7. Rock slide on the downslope face of the slump block (Fig. 9). Mapped structures define the moderately sized (~11,000 m^2) rock slide of phase 7, which cuts rock avalanche deposits on the western half of the face of the slump block. The timing of this rock slide is constrained between two DigitalGlobe WorldView-2 satellite images (http://global.digitalglobe.com/sites/default/files/DG_WorldView2_DS_PROD.pdf), one acquired prior to the rock slide on 7 June and the other after the rock slide on 18 August. A comparison of DEMs derived from this imagery revealed that the rock slide had well-developed source and toe areas with negative and positive elevation changes up to 10 m (Fig. 9) that conform with mapped structures.

Phase 8: Ongoing rock slides and falls from the headscarp. We observed numerous rock slides and rock falls from the headscarp (phase 8) during field work in the summer of 2014. We also noticed that a portion of the center of the headscarp (directly above the sag pond) retrogressed upslope by ~16 m (horizontal distance) between mid-June and mid-July 2014. One large rock slide on 11 July 2014 fell into the south side of the sag pond and created a wave that traveled ~5 m (vertical distance) up the south side of the slump block, damaging a monitoring station, leaving small pools of water in depressions, and flattening grass growing on the bank.

Thickness and Volume

For estimates of thickness and volume, we concentrated on the back-rotated rock slide (phase 2) and the rock avalanche (with phases 1 and 3–7 lumped together). Thickness is highly variable, with the rock slide having a maximum thickness of ~155 m and the avalanche deposit ranging from negative and positive values near 0 at the head of the deposit to a maximum of ~38 m thick in the central core above the toe (Fig. 10). The yellow color in Figure 10 shows areas that are within the estimated vertical error of the 10 m DEM (±4.72 m). Negative values <–4.72 m indicate that some erosion and entrainment of materials occurred in the area near the head of the avalanche deposit, particularly along the east flank, but also along the valley floor where ponds were located prior to the event. Erosion and entrainment were also probable within the yellow areas, but could not be confirmed from the DEM analysis or from field work.

The total volume of both the rock slide and rock avalanche is 54.5 ± 13.0 Mm^3, with 43.0 ± 12.9 Mm^3 in the rock slide block and 11.5 ± 0.1 Mm^3 in the avalanche deposit. A comparison of these volumes combined with the previously described *L*/*H* mobility index value (7.22) versus volumes and *L*/*H* values from other landslides indicates that the relative mobility of the West Salt Creek rock avalanche was high (Fig. 11). We did not estimate a volume for ongoing rock slides and rock falls from the headscarp because a large portion of rock from these events was underwater in the sag pond.

Hummocks

Hummocks were formed along the length of the avalanche during phases 2 through 4 (Figs. 12A and 12C). The highest concentrations of hummocks were on the slump block at distances between 200 and 600 m from the headscarp and in the avalanche deposit between 1200 and 2000 m and between 2600 and 3600 m from the headscarp (Fig. 12C). The lowest concentrations were located on the steep downslope face of the slump block, at the narrowest part of the central avalanche core, and near the toe. The majority (~60%) of hummocks had areas <20 m^2 (Fig. 12B). The largest hummock was in the central core and had an area of 3112 m^2 (Fig. 8E). The majority (60%) of hummocks were on slopes between 5° and 15° (determined from the pre-avalanche 10 m DEM; Fig. 12D), and 78% of hummocks were in areas where the thickness of the avalanche deposit was 35 m or less (Fig. 12E).

Seismic Analysis

Seismic waves were observed for phases 1 through 3, described above, and provide additional constraints on the timing and dynamics of each phase, as well as velocity estimates. The first seismic signals on 25 May were associated with the early morning event described by Slug Hawkins as a "strange hissing noise" (phase 1). Faint high-frequency signals lasting just over a

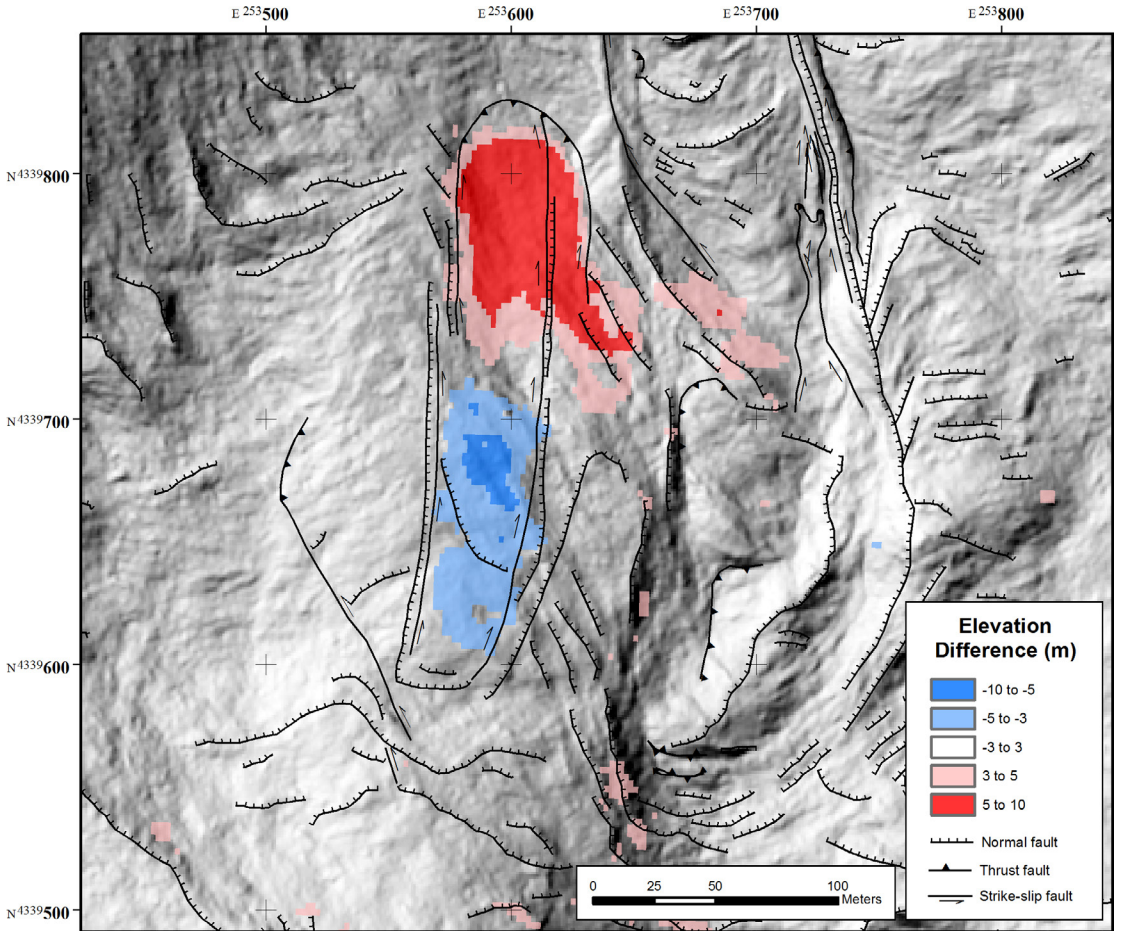

Figure 9. Rock slide (movement phase 7; see Fig. 7). Elevation difference from digital elevation models (DEMs) derived from DigitalGlobe WorldView-2 satellite imagery (18 August 2014 DEM minus 7 June 2014 DEM). Structures are from field mapping. Lidar base was acquired prior to rock-slide movement. The coordinates shown are UTM zone 13.

minute were observable at short-period stations as far away as 141 km with a start time of 13:19 UTC (07:19 local time). Weak long-period signals (period > 25 s) associated with the event were noted as far away as 181 km, but signal-to-noise ratios were too low to invert the waveforms for a robust force history. However, the fact that long-period signals accompanied by high frequencies were observable at great distances, and lasted only a minute, indicates an energetic event that most likely had landslide and debris-flow components (i.e., phase 1). The energetic event was followed by the slow movements observed by Slug Hawkins. The long-period signal shows up most clearly on the vertical component of the closest broadband station, O20A (Fig. 6). The waveform is similar to that of the main rock slide and rock avalanche later in the day (phases 2 and 3) but with peak velocity amplitudes two orders of magnitude smaller (3 nm/s versus 150 nm/s). If this initial event had a similar failure mechanism and thus a similar acceleration time history to the main rock slide and avalanche—a reasonable assumption given the similarity of the waveforms—this would suggest that the landslide mass was about two orders of magnitude smaller than that of the main rock slide and rock avalanche.

The rock slide and rock avalanche (phases 2 and 3) were recorded much more broadly and with much higher amplitudes. The high frequencies recorded at the closest station (WOY.ELZ.NF at 31.8 km) emerged from the noise at ~23:43:46 UTC (17:43:46 local time) and lasted just over 3 min. However, because the high frequencies are emergent, i.e., take time to build, and are delayed due to travel times, the best estimate of the start time and duration comes from the landslide force history.

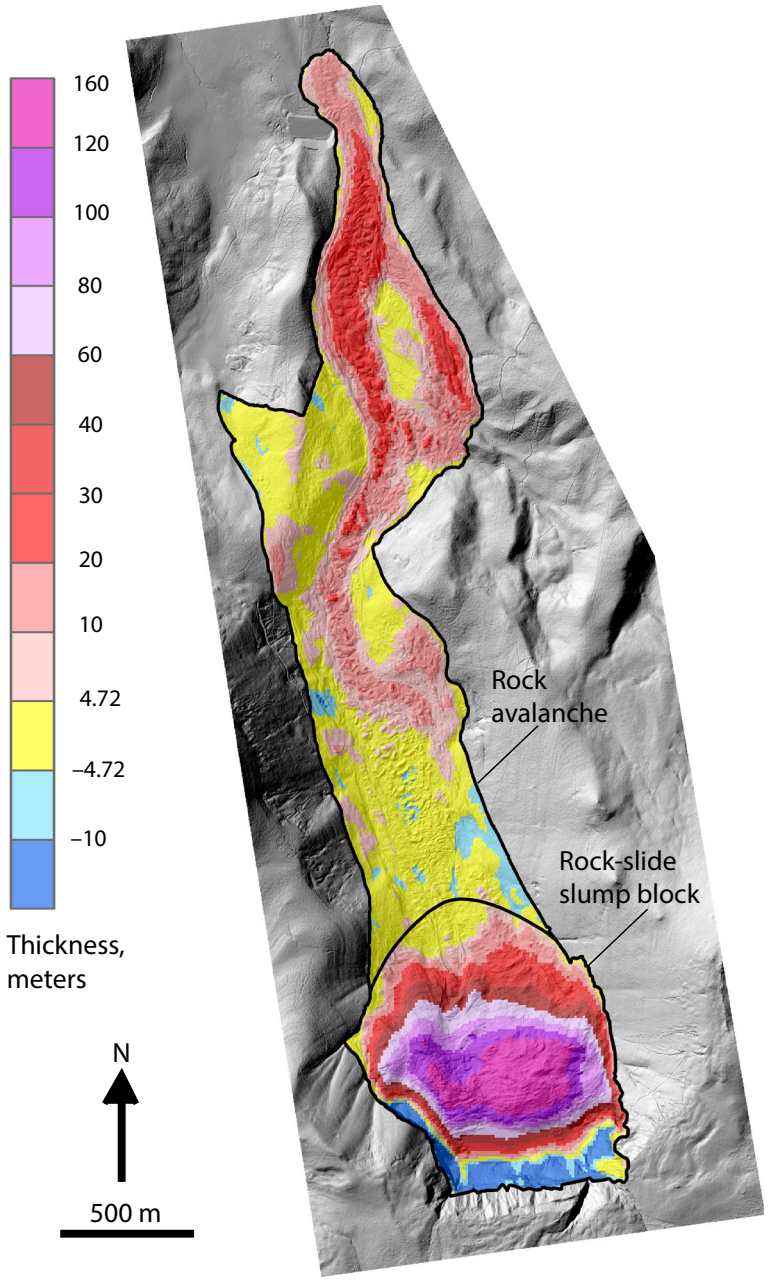

Figure 10. Thickness map overlain on shaded-relief lidar data.

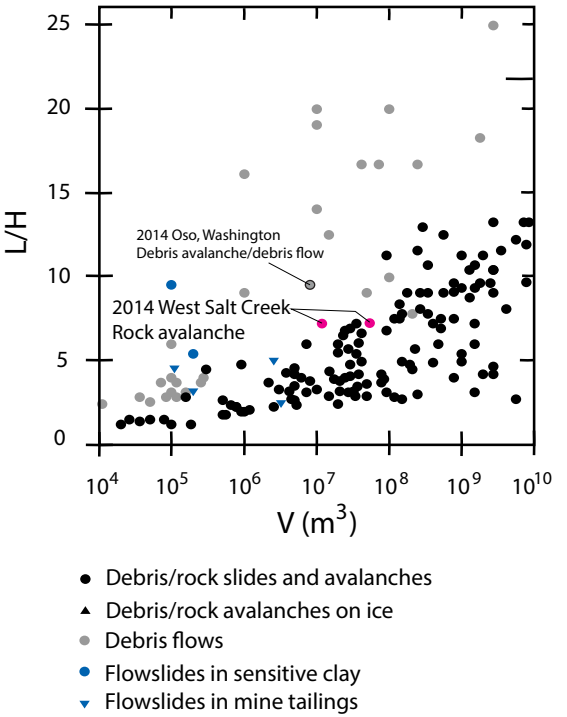

Figure 11. Comparison of mobility index values (L is the maximum length traveled, H is the maximum elevation traveled, and V is landslide volume) for the West Salt Creek rock avalanche with those of other fast-moving landslides (modified from Iverson et al. [2015] using data from Carasco-Nunez et al. [1993], Corominas [1996], Iverson [1997], Dawson et al. [1998], Legros [2002], and Zanchetta et al. [2004]). Two dots for West Salt Creek represent the total combined volume of the slump block and mobilized rock avalanche (54.5 ± 13.0 Mm^3) and volume of the mobilized rock avalanche alone (11.5 ± 0.1 Mm^3). The recent Oso, Washington, debris avalanche is shown for reference. Sensitive clay is a type of clay that is prone to a sudden loss of strength when it is disturbed.

The landslide force history derived from seismic inversion is shown on Figure 13A, with the shading indicating uncertainties, and data and fit of the solution shown in Figure 6. The variance reduction of this solution is 64%. The zero time of the force history is 23:43:32 UTC (17:43:32 local time). The segments of the central avalanche path corresponding to each interval of the force history (a–h) are shown in Figure 13C. The peak horizontal vectors are plotted at geographic locations of peak forcing. The horizontal azimuth of the peak force of the first interval, interval a, points directly upslope from the source area (Fig. 13C) with a vertical angle of ~10°. This is consistent with the initial acceleration of the rock-slide slump block (phase 2). After ~20 s the horizontal azimuth flips ~180° during interval b, to a direction consistent with deceleration of the slump block.

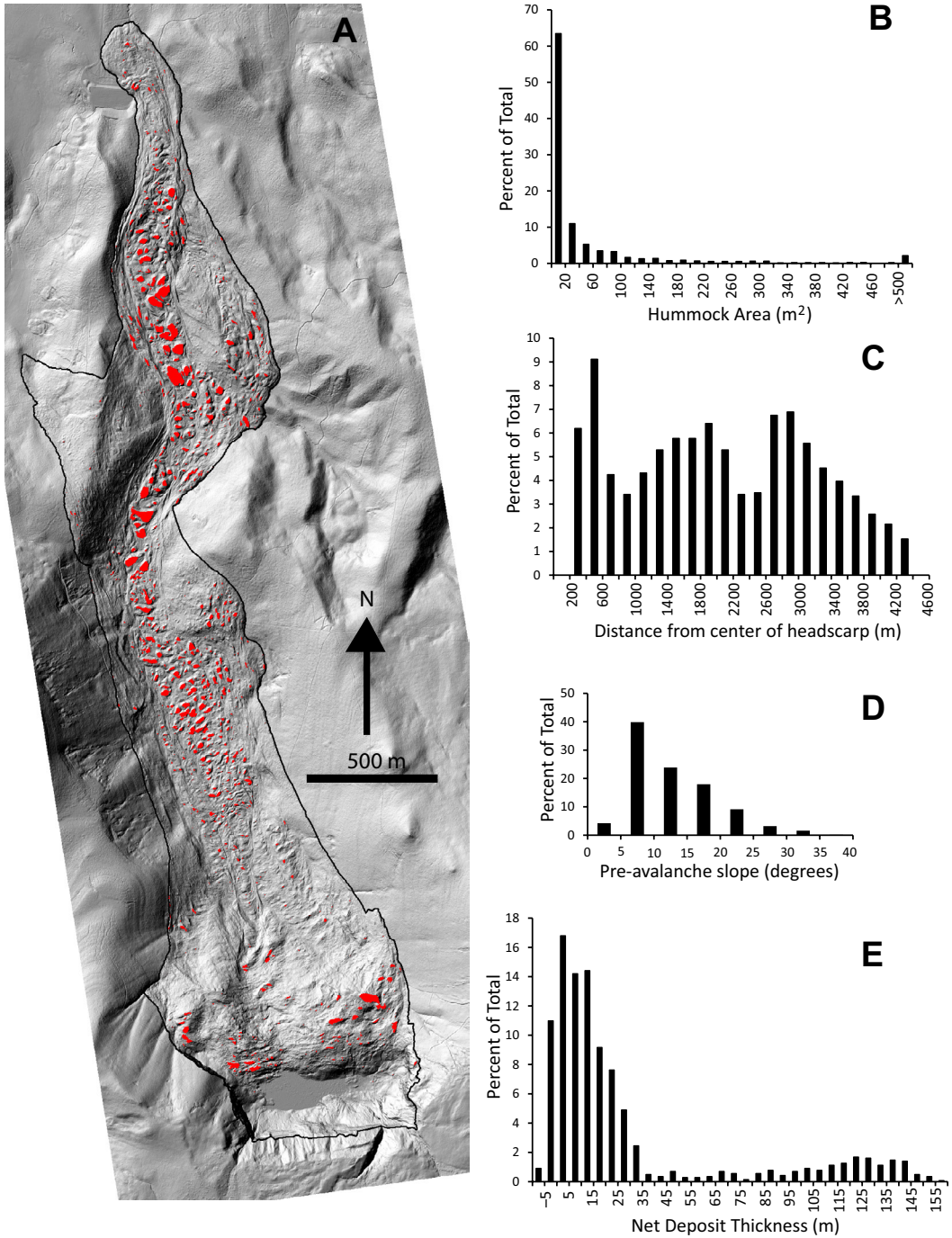

Figure 12. (A) Map of hummocks (red) on the surface of the West Salt Creek rock avalanche. (B-E) Hummock statistics.

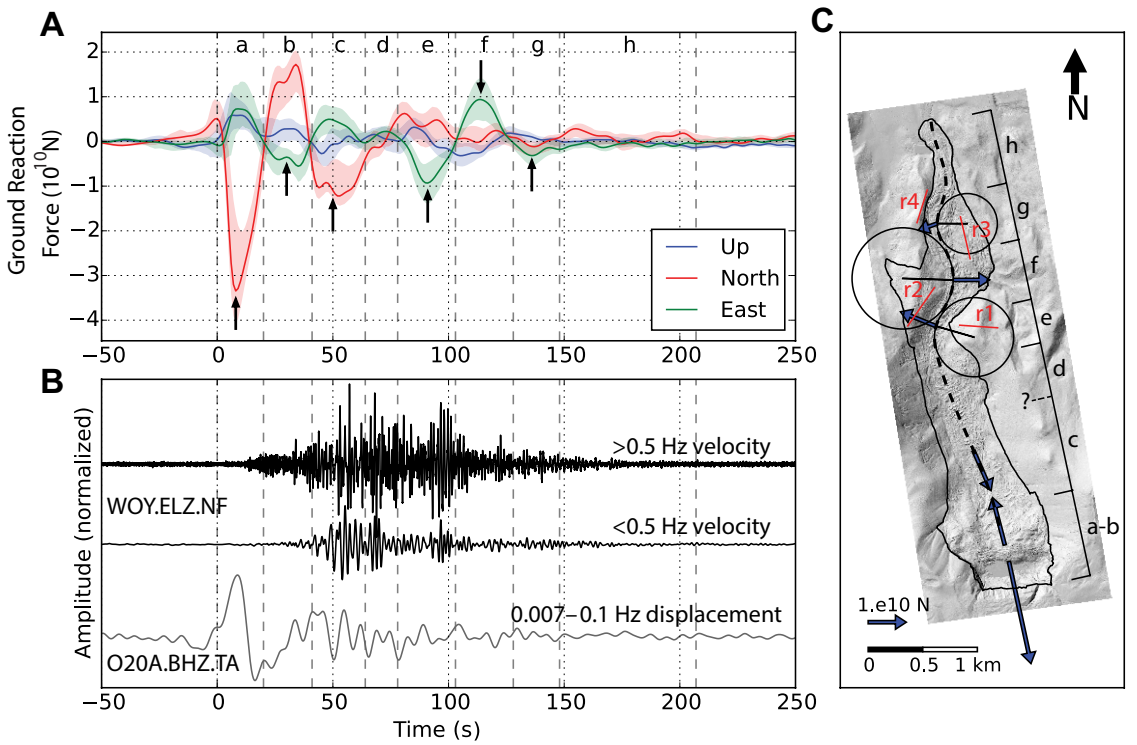

Figure 13. (A) Time series of forces exerted on the earth (force history) due to landslide motion derived from seismic inversion. The best-fitting model is shown (solid lines) with shading indicating the confidence limits. Dashed lines delineate intervals corresponding approximately to segments of the path shown on C and described in the text. Small arrows show the interval peaks that are plotted as horizontal vectors on C. Time = 0 s corresponds to the start time of the rock slide (movement phase 2), 23:43:32 UTC (17:43:32 local time). (B) Velocity seismogram from one of the closest seismic stations, WOY.ELZ.NF, a short-period station located 31.7 km to the southeast, filtered to show just the highest frequencies (>0.5 Hz, top) and just the lowest frequencies (<0.5 Hz, bottom). Below that is the displacement seismogram from the closest broadband station, O20A.BHZ.TA, at periods of 10–150 s. The data are adjusted backward for approximate travel times by 18 s and 43 s for stations WOY.ELZ.NF and O20A.BHZ.TA, respectively, to roughly line up with the force history as explained in the Methods section. (C) Post-event lidar shaded-relief map showing the outline of deposits, approximate path, and vectors corresponding to peaks in the force history placed at their approximate corresponding geographic locations. These force vector peaks point opposite to the direction of acceleration (linear or centripetal). Circles are plotted at the point of peak curvature of the path with a radius equal to the radius of curvature in order to find the appropriate geographic location corresponding to the peak forces due to centripetal accelerations around curves. The peak forces should point exactly away from the center of the circle fit to the point of peak curvature if the location fit is good (e.g., vectors in intervals e and f), and they would not line up if the fit is less optimal (e.g., vector in interval g). Ridges 1–4 (r1–r4) mentioned in the text are indicated with red lines.

Some unusual features of the interval b force history (Fig. 13A) include an upward vertical force (usually the vertical force is down for a deceleration), a peak horizontal amplitude that is one-third lower than for acceleration, and a dip in the horizontal peak amplitude at the same time as the upward peak in the vertical force. One possible explanation is that while the slump block was decelerating, the rock avalanche that it spawned was mobilizing. This may have overprinted an acceleration signal over the larger signal from slump-block deceleration. The peak vectors for intervals a and b are plotted at the approximate location of the center of mass before and after the rock slide occurred, respectively (Fig. 13C).

After interval b, the azimuth of the horizontal vector points directly up the path for ~23 s (interval c), which is consistent with the acceleration of the rock avalanche (phase 3) down the initial open and straight part of the path. This is supported by the lack of significant deposition in this area (Fig. 10). The peak force in interval c is broad and consistent in azimuth and there is no specific feature along the path that could provide a geographic point to tie a peak vector to, so we placed the horizontal vector halfway down the length of the interval (Fig. 13C) and do not use this vector location for any velocity calculations. After interval c, the magnitude of force is near zero for ~14 s (interval d). In interval d, the avalanche was not accelerating or decelerating significantly, nor traveling through any bends in the valley. After interval d, there are two approximately east-west peaks (intervals e and f) that likely correspond to the material turning through two tight curves in the path. To tie the peak of each of these intervals of the force history to a geographic location, we calculated the point of peak curvature of the path and tied the peak forces for intervals e and f to these points. In theory, because these forces are due to centripetal acceleration, which points toward the center of the curve, the force should point directly away from the center of the curve (i.e., directly away from the center of a circle fit to the point of peak curvature). This is indeed the case within a few degrees for vectors e and f (Fig. 13C), which validates their placement at the assigned geographic points.

The beginning of interval e starts with a northward force followed by an upward force. Though uncertainties are high for these parts of the force history, this could reflect where the eastern part of the avalanche, moving at peak speeds, impacts the ridge that forms the first curve (r1, Fig. 13). In this case, the avalanche would have first decelerated horizontally (northward force) while accelerating upward over the ridge (not clearly seen in Fig. 13), but would then

have decelerated vertically as the material overrode the ridge (upward force, Fig. 13). Avalanche material also overrode the ridge at the second curve (r2, Fig. 13), but there is no comparable signal accompanying the strong eastward peak except a long-duration downward force followed by a long-duration upward force. The avalanche was slowing and depositing material along this path, so by interval g, the force amplitudes are low. By ~170 s after the start, the force history is not significantly different from zero, as indicated by the uncertainties (shaded regions, Fig. 13A), but the signal still remains elevated until 207 s. The high-frequency seismic signal also does not return to pre-event levels until about this point. So, for both reasons, 207 s (3.45 min) is our best estimate of the duration of the main rock slide–avalanche sequence (phases 2 and 3). This marks the end of the high-energy part of the event. Based on Eric Bruton's eyewitness account and on detailed mapping of strike-slip faults defining movement of the central core (phase 4), less-energetic motion occurred after this point, but it was not seismogenic.

The path length from the center of mass of the rock slide (the starting location of the southernmost vector in path segment a-b, Fig. 13C) to the end of the deposits along the path shown in Figure 13C is ~4.3 km. Based on this distance and our duration estimate for the high-energy avalanche, an estimate for the average velocity of the rock slide and avalanche (phases 2 and 3) is 21 m/s, with a possible range of 20–26 m/s. However, this is a rough estimate because it assumes that the entire avalanche travel distance was seismogenic, which was likely not the case as suggested by Eric Bruton's observations of continued slower motion after the main rock avalanche. We computed more accurate estimates of velocities for individual segments of the path between well-constrained geographic points tied to force history peaks (Fig. 13). These estimates and their possible ranges are shown in Table 4.

The average velocity from the center of the rock slide to the first curve is 26 m/s (a range of 24–28 m/s), but that includes the rock slide starting from zero. If we isolate just the rock avalanche before it enters the curves and assume that it starts at the north end of the b vector (the northern vector in path segment a-b, Fig. 13C), the average velocity is 36 m/s (32–41 m/s). The peak velocity, which would be >36 m/s, would have occurred within this segment. Once the material enters the curves, average velocities drop to 20 m/s (10–31 m/s) between the first two curves, e and f, and to 17 m/s (15–33 m/s) from curve f to the end of the path. The geographic location of the peak force of interval g is poorly constrained, but if we use it, it gives estimates of 25 m/s (14–39 m/s) between f and g. It is unlikely that the velocity actually increased here, so this suggests that the geographic location we use for the peak of interval g may be too far down the path, and the actual average velocity was probably closer to the lower end of the range (i.e., 14 m/s).

Figure 13B shows that interval a (the rock slide, phase 2) was not accompanied by any observable high-frequency energy; this interval is dominated by long-period energy. This trait is typical for initial acceleration (e.g., Allstadt, 2013a; Hibert et al., 2014) because it takes time for the momentum, agitation, and frictional work rate to build—all factors that are thought to contribute to the generation of high-frequency energy (e.g., Huang et al., 2007; Schneider et al., 2010; Hibert et al., 2014). The high frequencies start to appear during interval b as the slump block decelerates, but only in the >0.5 Hz frequency range. The peak in high-frequency energy corresponds to acceleration and propagation of the main avalanche (phase 3) along the initial straight path (interval c-d, Fig. 13C). The reason for the high-frequency energy could be that velocities are highest (more energy, individual impacts), or that frictional processes started to become more prevalent toward the end of interval c and into d, where material is starting to be deposited. The high-frequency energy increases again as it passes through interval e, potentially due to increased agitation of avalanche material as it impacts topography in this curve (e.g., Moretti et al., 2015). High-frequency energy then decreases through interval g, indicating a loss of volume as material is deposited.

DISCUSSION

Our detailed forensic work at West Salt Creek shows that the rock avalanche was a cascading sequence of landslide events, rather than a single massive failure. Individual landslide phases modified previous structures,

TABLE 4. ESTIMATED ROCK-AVALANCHE VELOCITIES

Segment	Start time (s)	Possible range (s)	End time (s)	Possible range (s)	Duration (s)	Possible range (s)	Distance along path (m)	Possible range (m)	Average velocity (m/s)	Possible range (m/s)
Entire path	0	–2 to 1	207	170–209	207	169–211	4300	4175–4425	21	20–26
Start to peak E	0	–2 to 1	91	90–92	91	89–94	2350	2225–2475	26	24–28
Peak B to peak E	30	28–33	91	90–92	61	57–64	2195	2070–2320	36	32–41
Peak E to peak F	91	90–92	114	113–115	23	21–25	450	250–650	20	10–31
Peak F to peak G	114	113–115	136	134–138	22	19–25	550	350–750	25	14–39
Peak F to end	114	113–115	207	170–209	93	55–96	1600	1400–1800	17	15–33
Peak G to end	136	134–138	207	170–209	71	32–75	1030	830–1230	15	11–38

Note: Peaks in the first column refer to peaks in each interval of the force history as shown by small arrows in Figure 13A. Possible range indicates the range of possible values based on confidence limits shown by shading in Figure 13A.

deposits, and morphology, and in the case of movement of the central core, modified the apparent travel distance of the main rock avalanche. Attributing all deposits and structures to a single massive failure would be inaccurate and could yield misplaced interpretations of avalanche mechanics, dynamics, mobility, and hazards.

Our interpretation of structures from the main avalanche indicates that the avalanche had the mobility of a fluid but, at least at the near surface, deformed by both distributed and discrete shearing in frictionally strong material. For example, the initial avalanche front was thick (~40 m), rapidly moving (~36 m/s), and left "flow" bands indicative of distributed shear and fluid-like behavior. This front traveled ~3500 m (~75% of the total length of the avalanche) along the valley floor with slope gradients ≤10°. However, all structures on the surface of the avalanche that formed after the passage of this initial front indicate that the avalanche internally deformed predominantly by sliding along well-defined, discrete shear surfaces in material that was dry and had substantial frictional strength. The broad distribution of structures (Supplemental Figure) and back-tilted hummocks indicates that frictional strength existed throughout multiple phases of movement, including the main avalanche, central core of the avalanche, and subsequent landslide and rock-slide failures in the avalanche deposit.

These observations suggest that mobility of the main rock avalanche (and the central core) was likely enhanced by liquefaction of material along the valley floor caused by undrained loading (Hutchinson and Bhandari, 1971; Sassa, 1985; Sassa,et al., 2004; Hungr and Evans, 2004) by the overriding avalanche. Three pieces of evidence support this interpretation: the pre- and post-avalanche debris flows, the presence of the pre-event stream and ponds along the valley floor, and the occurrence of the avalanche during a rain-on-snow event at the peak of the snowmelt and surface-water runoff season. Buss and Heim (1881) suggested a similar mechanism at the Elm avalanche in Switzerland, as have numerous authors thereafter (Voight and Sousa, 1994; Hungr and Evans, 2004; Huggel et al., 2005; Evans et al., 2007; Xu et al., 2012). This interpretation is in agreement with the conclusion of Hungr and Evans (2004) that the mobility of many avalanches is enhanced by liquefied basal materials. These results suggest that the West Salt Creek avalanche, and many other avalanches, could ideally be modeled as two layers: a liquefied basal layer and a much thicker and stronger overriding layer. Most avalanche modeling studies have used one layer and either (1) performed scenario simulations to investigate the effects of varying material conditions on avalanche mobility (e.g., Crosta et al., 2009; Iverson et al., 2015) or (2) varied the rheology of the layer along the flow path to correspond with areas of basal liquefaction (e.g., Hungr and Evans, 2004; Evans et al., 2007). Any new two-layer modeling effort should consider the constraints for two-layer models recently outlined by Iverson and Ouyang (2015).

Our estimates of average avalanche velocities from the seismically derived force history can be compared to the independently estimated velocities of White et al. (2015). White et al. (2015) used several different conventional methods to estimate velocities, including an often-used theoretical method based on field measurements of super-elevation (i.e., the forced vortex equation of Chow [1959]). Though their velocities are not directly comparable with ours because their method estimates peak velocity at a point along the path and ours estimates the average velocity along intervals of the path, the velocities should still be compatible if both methods are valid. This is largely the case. For example, their peak-velocity estimate for the peak curve within interval e (Fig. 13) is 37 m/s. This is nearly identical to our estimate of the average velocity along the path prior to this point (b to e, 36 m/s, Table 4). The actual peak velocity based on our interpretation is probably higher than their estimate of 37 m/s because our average includes the initiation of the rock avalanche from near 0 m/s. However, velocities probably started decreasing before reaching interval e because the avalanche was likely slowed by the first ridge (r1 on Fig. 13) and deposition started prior to this interval. Their peak-velocity estimate within interval f (Fig. 13) is 19–29 m/s depending on two possible interpretations of deposits. Our estimate of average velocity for e to f is 20 m/s. Finally, White et al. (2015) estimated speeds of 9 m/s within interval g. This is much lower than our estimate of average velocity from f to g (25 m/s), or even from g to the end of the deposit (15 m/s). It is difficult to say which estimate is more reliable at this location. The super-elevation method may yield inaccurate results at this location because ridge 3 (r3, Fig. 13) may have influenced super-elevation heights. Our estimates may be too high because we do not know where the end of the seismogenic part of the path is located and we suspect that our methods place the geographic location for the peak force of interval g too far down the path. The lower end of our velocity range for f to g (14 m/s, Table 4) is probably most realistic.

Our results also have implications for mapping and interpreting paleolandslide deposits. In these deposits, many of the original structures will no longer be visible or could be inaccurately grouped and interpreted as a single massive failure. Other landslide researchers have noted how fast field evidence in avalanche deposits disappears (e.g., Carey et al., 2015). Our visits to West Salt Creek over the winter and spring of 2014–2015 indicate that the topographic distinctness of many structures is rapidly degrading due to degradation (slaking) of broken shale clasts of the Green River Formation and that vegetation is beginning to reestablish itself. These observations highlight the importance of using caution when interpreting structures in paleolandslide deposits and conducting field work as soon as possible after an avalanche event. At West Salt Creek in semi-arid Colorado, the window of mapping opportunity lasted ~6 mo after the event.

That said, if avalanche topography or deposit characteristics were long lasting, then detailed structure and deposit maps such as ours could potentially be used to interpret emplacement characteristics of paleolandslides. For example, our map might be useful for interpreting whether emplacement velocities of paleolandslide deposits were fast or slow. From a hazard point of view, the key question should be: Did the paleolandslide travel at a velocity faster or slower than humans can run (~6 m/s)? This can be a very difficult question to answer because there are few guidelines that can be used to interpret the emplacement velocity of paleolandslide deposits. Commonly used mobility indices (e.g., H/L or L/H) are not necessarily useful for interpreting

landslide velocity. For example, there are many long-traveled earth flows that moved at slow (centimeters to meters per day) velocities (e.g., the Slumgullion earth flow: Fleming et al., 1999, Coe et al., 2003; the Montaguto earth flow: Guerriero et al., 2013, 2014). A comparison of structures and deposits at West Salt Creek, for which we have seismically constrained velocity ranges, to structures mapped at these slow-moving earth flows could provide guidelines for estimating velocities of other long-traveled paleolandslide deposits. A preliminary comparison suggests that the high-velocity West Salt Creek avalanche contained the following features (Figs. 7 and 12; Supplemental Figure) that the slow-moving earth flows did not: (1) internal strike-slip faults (topographic furrows) and lateral deposits with abrupt changes in their strike direction; (2) an extensive field of back-rotated, concentric- to oblate-shaped hummocks on the lower half of the deposit; (3) elongated tongue-shaped internal deposits; (4) extensive "flow" banding; (5) extensive thin (0–2 m) deposits cut by normal faults along valley flanks and on preexisting ridges along and within the travel path; and (6) no trees that survived the rapid movement intact and abundant piles of downed trees on the surface of the deposit. Additional detailed mapping of fast- and slow-moving landslides will be needed to confirm these observed differences. If the observations are consistent, they may serve as an initial set of guidelines to at least crudely estimate the velocity of paleolandslide deposits.

Additionally, from a hazard point of view, the West Salt Creek avalanche gave off warning signs prior to the catastrophic failure. Specifically, the landslide and debris flow that occurred ~10 h before the main rock avalanche were a precursor of the larger event. Although precursor events are commonly not detected, we are confident that other rock and debris avalanches have such events. One such event was the 2009 Nile Valley landslide in Washington State (United States), where seismically observable precursory landslides occurred the day prior to a rapid 10^7 m^3 landslide. No landslide monitoring system existed, but fortunately residents heard and saw precursory rock falls and safely evacuated before the event destroyed several of their houses (Allstadt, 2013b). Another example is Iliamna volcano in Alaska (United States), where frequent rock and ice avalanches are commonly preceded by several hours of precursory seismicity (Caplan-Auerbach and Huggel, 2007). In the United Kingdom, repeat laser scanning of coastal cliffs revealed precursor rock-fall activity prior to large rock-slope failures (Rosser et al., 2007). If precursory events, or even the initiation of events with long travel distances, could be seismically identified and placed in the proper context, they could potentially be used for early warning purposes.

Our results beg the question: How many other existing and/or future rock-avalanche deposits and accompanying seismic recordings could be studied to better understand avalanche mechanisms, dynamics, and mobility? Smaller-scale mapping at numerous volcanic debris avalanches by Shea and van Wyk de Vries (2008) and at earthquake-triggered rock avalanches by Schulz et al. (2008) suggest that most rock-avalanche deposits probably contain structures and/or flow banding, and that maps of these features are important in deciphering avalanche sequencing and dynamics. At this point, however, there are very few structure maps that can be used to compare and contrast avalanches with varying styles of failure and differing levels of mobility. More field-based maps are needed so such comparisons are possible. Recent analyses of seismic signals from rock and debris avalanches (e.g., Deparis et al., 2008; Ekstrom and Stark, 2013) indicate that the number of seismic records of avalanches is large and continually increasing. The potential for new and insightful analyses of these data, when integrated with field mapping, modeling, and other analyses, seems unlimited.

CONCLUSIONS

Our detailed mapping and seismic analysis at the West Salt Creek rock avalanche lead us to the following conclusions.

The rock avalanche was induced by a rain-on-snow event on 25 May 2014 during the peak of the spring snowmelt season. The rainfall was not exceptional; 0.25, 0.5, 1, 2, 6, and 24 h accumulations of rainfall had estimated return periods of <2 yr. Snowpack, cumulative precipitation, and runoff were also not exceptional, as all were below historical averages. The rainfall was unusual simply because it fell on snow at high elevations (2750–2900 m) at the head of West Salt Creek.

The rock avalanche was a series of eight landslide movement phases that began ~10 h before the main rock avalanche occurred and are still ongoing (as of September 2015). These phases, in chronological order, include a (1) landslide/debris flow, (2) a rock slide/back-rotated slump block that spawned the main rock avalanche, (3) the main rock avalanche from the downhill face of the slump block, (4) slow movement of the central core of the rock avalanche, (5) shallow landslides in steep rock-avalanche deposits, (6) a second debris flow, (7) a rock slide on the steep downhill face of the slump block, and (8) ongoing rock slides and rock falls from the oversteepened headscarp of the rock slide/slump block. Hummocks formed along the length of the avalanche during landslide movement phases 2 through 4.

The main rock avalanche lasted ~3.5 min and traveled ~4.3 km at estimated velocities ranging from 11 to 41 m/s (40–148 km/h). The total volume of the slump block and mobilized rock avalanche was 54.5 ± 13.0 Mm^3, with 43.0 ± 12.9 Mm^3 in the slump block and 11.5 ± 0.1 Mm^3 in the avalanche deposit. About 75% of the travel path had slope gradients ≤10°.

The avalanche had the mobility of a fluid, but mapped structures indicate that it deformed at and near the surface by both distributed and discrete shearing in frictionally strong material. The mobility of the rock avalanche was likely enhanced by liquefaction of wet valley floor sediments. Additionally, pre- and post-event DEM differencing indicated that material immediately downslope from the face of the slump block was entrained by the avalanche. Entrainment of material at other locations along the flow path was possible, but could not be verified.

The implications of our work are that: (1) the West Salt Creek avalanche, and probably many other avalanches, could ideally be modeled as two layers,

a liquefied basal layer and a much thicker and stronger overriding layer; (2) detailed structure maps such as ours could be useful for interpreting the velocity characteristics of paleolandslides; and (3) if precursor events, such as the one at West Salt Creek that occurred ~10 h before the main avalanche, could be seismically detected and placed in the proper context, they could possibly be used for avalanche warnings.

ACKNOWLEDGMENTS

We thank the Hawkins family, specifically Jerald and Slug Hawkins, for allowing us to work on the Hawkins Ranch property. We are grateful to Andy Martsolf, Jim Fogg, Garrett Jackson, Benjamin Miller, Aldis Strautins, Pete Baier, David Brown, Erin Gleason, Eric Brantingham, and Mike Meininger for coordination and collaboration during emergency-response activities in late May and early June 2014; Bill Edwards of the U.S. Forest Service for the initial invitation to work at West Salt Creek; and Karen Berry, Ed Harp, Dennis Staley, Paul Santi, and Jonathan Godt for collaborative support during emergency-response work. Mark Fahey, Beverly Friesen, Christopher Cole, and Earl Wilson provided rectified Digital Globe images and associated DEM data. Conversations with Rex Cole, Verner Johnson, Mark Reid, Bill Schulz, and Brian Collins provided helpful insights throughout our work. We thank David George, Jill McCarthy, Janet Slate, Jonathan Godt, Associate Editor Colin Amos, Jeffrey Moore, an anonymous reviewer, and Raymond Russo for their constructive comments on this paper.

This work was partially supported by the National Science Foundation under award number 1349572. The facilities of Incorporated Research Institutions for Seismology (IRIS) Data Services (Seattle, Washington), and specifically the IRIS Data Management Center, were used for access to waveforms, related metadata, and/or derived products used in this study. IRIS Data Services are funded through the Seismological Facilities for the Advancement of Geoscience and EarthScope (SAGE) Proposal of the National Science Foundation under Cooperative Agreement EAR-1261681. Seismic data accessed through IRIS came from the USArray Transportable Array, the University of Utah Regional/Urban Seismic Network, the Intermountain West Seismic Network, the Arizona Broadband Seismic Network, and the United States National Seismic Network. Additional data from private networks were kindly provided by the North Fork Valley Seismic Network courtesy of Peter Swanson, and the Paradox Valley Seismic Network through the U.S. Bureau of Reclamation Colorado River Basin Salinity Control Project. Data from the Transportable Array network were made freely available as part of the EarthScope USArray facility, operated by IRIS and supported by the National Science Foundation under Cooperative Agreement EAR-1261681. Financial support was provided by the USGS, including the Landslide Hazards Program, and the Advanced National Seismic System (ANSS) and the State of Utah. Intermountain West network data are freely available from the USGS Earthquake Hazards Program. Any use of trade, product, or firm names is for descriptive purposes only and does not imply endorsement by the U.S. Government.

REFERENCES CITED

Allstadt, K., 2013a, Extracting source characteristics and dynamics of the August 2010 Mount Meager landslide from broadband seismograms: Journal of Geophysical Research, v. 118, p. 1472–1490, doi:10.1002/jgrf.20110.

Allstadt, K.E., 2013b, Surficial seismology: Landslides, glaciers, and volcanoes in the Pacific Northwest through a seismic lens [Ph.D. thesis]: Seattle, University of Washington, 213 p.

Aslan, A., Karlstrom, K.E., Crossey, L.J., Kelley, S., Cole, R., Lazear, G., and Darling, A., 2010, Late Cenozoic evolution of the Colorado Rockies: Evidence for Neogene uplift and drainage integration, *in* Morgan, L.A., and Quane, S.L., eds., Through the Generations: Geologic and Anthropogenic Field Excursions in the Rocky Mountains from Modern to Ancient: Geological Society of America Field Guide 18, p. 21–54, doi:10.1130/2010.0018(02).

Bartelt, P., Bühler, Y., Buser, O., Christen, M., and Meier, L., 2012, Modeling mass-dependent flow regime transitions to predict the stopping and depositional behavior of snow avalanches: Journal of Geophysical Research, v. 117, F01015, doi:10.1029/2010JF001957.

Baum, R.L., and Fleming, R.W., 1991, Use of longitudinal strain in identifying driving and resisting elements of landslides: Geological Society of America Bulletin, v. 103, p. 1121–1132, doi:10.1130/0016-7606(1991)103<1121:UOLSII>2.3.CO;2.

Baum, R.L., and Odum, J.K., 1996, Geologic map of slump-block deposits in part of the Grand Mesa area, Delta and Mesa Counties, Colorado: U.S. Geological Survey Open-File Report 96-017, 12 p., 2 oversize plates, scale 1:24,000.

Baum, R.L., and Odum, J.K., 2003, Retrogressive slumping at Grand Mesa, Colorado, *in* Boyer, D.D., Santi, P.M., and Rogers, W.P., eds., Engineering Geology in Colorado: Contributions, Trends, and Case Histories: Association of Engineering Geologists Special Publication 15 and Colorado Geological Survey Special Publication 55, available on CD-ROM (not paginated), 17 p.

Berrocal, J., Espinosa, A.F., and Galdos, J., 1978, Seismological and geological aspects of the Mantaro landslide in Peru: Nature, v. 275, p. 533–536, doi:10.1038/275533a0.

Bradley, W.H., 1931, Origin and microfossils of the oil shale of the Green River Formation of Colorado and Utah: U.S. Geological Survey Professional Paper 168, 58 p.

Bridge, T., 2014, Mesa County Deputy Sheriff activity report, June 9, 2014, case number 2014-15096: Grand Junction, Colorado, Mesa County Sheriff's Office.

Brodsky, E.E., Gordeev, E., and Kanamori, H., 2003, Landslide basal friction as measured by seismic waves: Geophysical Research Letters, v. 30, 2236, doi:10.1029/2003GL018485.

Buss, E., and Heim, A., 1881, Der Bergsturz von Elm: Zurich, Worster, 133 p.

Caplan-Auerbach, J., and Huggel, C., 2007, Precursory seismicity associated with frequent, large ice avalanches on Iliamna volcano, Alaska, USA: Journal of Glaciology, v. 53, p. 128–140, doi:10.3189/172756507781833866.

Carasco-Nunez, G., Vallance, J.W., and Rose, W.I., 1993, A voluminous avalanche-induced lahar from Citaltépetl volcano, Mexico: Implications for hazard assessment: Journal of Volcanology and Geothermal Research, v. 59, p. 35–46, doi:10.1016/0377-0273(93)90076-4.

Carey, J.M., Hancox, G.T., and McSaveney, M.J., 2015, The January 2013 Wanganui River debris flood resulting from a large rock avalanche from Mt Evans, Westland, New Zealand: Landslides, v. 12, p. 961–972, doi:10.1007/s10346-015-0607-0.

Chen, W.F., 1975, Limit Analysis and Soil Plasticity: Amsterdam, Elsevier, Developments in Geotechnical Engineering, v. 7, 638 p.

Chleborad, A.F., 1998, Use of air temperature data to anticipate the onset of snowmelt-season landslides: U.S. Geological Survey Open-File Report 98-124, 16 p.

Chow, V.T., 1959, Open-Channel Hydraulics: New York, McGraw-Hill, 680 p.

Coe, J.A., Glancy, P.A., and Whitney, J.W., 1997, Volumetric analysis and hydrologic characterization of a modern debris flow near Yucca Mountain, Nevada: Geomorphology, v. 20, p. 11–28, doi:10.1016/S0169-555X(97)00008-1.

Coe, J.A., Ellis, W.L., Godt, J.W., Savage, W.Z., Savage, J.E., Michael, J.A., Kibler, J.D., Powers, P.S., Lidke, D.J., and Debray, S.P., 2003, Seasonal movement of the Slumgullion landslide as determined from Global Positioning System surveys and field instrumentation, July 1998–March, 2002: Engineering Geology, v. 68, p. 67–101, doi:10.1016/S0013-7952(02)00199-0.

Coe, J.A., McKenna, J.P., Godt, J.W., and Baum, R.L., 2009, Basal-topographic control of stationary ponds on a continuously moving landslide: Earth Surface Processes and Landforms, v. 34, p. 264–279, doi:10.1002/esp.1721.

Cole, R.D., 2011, Significance of the Grand Mesa basalt field in western Colorado for defining the early history of the upper Colorado River, *in* Beard, L.S., Karlstrom, K.E., Young, R.E., and Billingsley, G.H., eds., CREvolution 2—Origin and Evolution of the Colorado River System, Workshop Abstracts: U.S. Geological Survey Open-File Report 2011-1210, p. 55–61.

Cole, R.D., and Sexton, J.L., 1981, Pleistocene surficial deposits of the Grand Mesa area, Colorado, *in* Epis, R.C., and Callender, J.F., eds., Western Slope Colorado: New Mexico Geological Society 32nd Field Conference Guidebook, p. 121–126.

Cole, R.D., Daub, G.J., and Weston, L.K., 1995, Review of geology, mineral resources, and ground-water of Green River Formation, north-central Piceance Creek Basin, Colorado, *in* Alverett, W.R., ed., The Green River Formation in Piceance Creek and Eastern Uinta Basins Field Trip: Grand Junction, Colorado, Grand Junction Geological Society, p. 63–82.

Corominas, J., 1996, The angle of reach as a mobility index for small and large landslides: Canadian Geotechnical Journal, v. 33, p. 260–271, doi:10.1139/t96-005.

Crosta, G.B., Imposimato, S., and Roddeman, D., 2009, Numerical modelling of entrainment/deposition in rock and debris-avalanches: Engineering Geology, v. 109, p. 135–145, doi:10.1016/j.enggeo.2008.10.004.

Dahlen, F.H., 1993, Single-force representation of shallow landslide sources: Bulletin of the Seismological Society of America, v. 83, p. 130–143.

Davies, T.R.H., 1982, Spreading of rock avalanche debris by mechanical fluidization: Rock Mechanics, v. 15, p. 9–24, doi:10.1007/BF01239474.

Dawson, R.F., Morgenstern, N.R., and Stokes, A.W., 1998, Liquefaction flowslides in Rocky Mountain coal mine waste dumps: Canadian Geotechnical Journal, v. 35, p. 328–343, doi:10.1139/t98-009.

Denlinger, R.P., 2014, Simulation of initiation, transport, and deposition of granular avalanches: Current progress and future challenges: Procedia IUTAM, v. 10, p. 363–371, doi:10.1016/j.piutam.2014.01.031.

Denlinger, R.P., and Iverson, R.M., 2001, Flow of variably fluidized granular masses across three-dimensional terrain: 2. Numerical predictions and experimental tests: Journal of Geophysical Research, v. 106, p. 553–566, doi:10.1029/2000JB900330.

Deparis, J., Jongmans, D., Cotton, F., Baillet, L., Thouvenor, F., and Hantz, D., 2008, Analysis of rock-fall and rock-fall avalanche seismograms in the French Alps: Bulletin of the Seismological Society of America, v. 98, p. 1781–1796, doi:10.1785/0120070082.

Eissler, H.K., and Kanamori, H., 1987, A single-force model for the 1975 Kalapana, Hawaii, earthquake: Journal of Geophysical Research, v. 92, p. 4827–4836, doi:10.1029/JB092iB06p04827.

Ekstrom, G., and Stark, C.P., 2013, Simple scaling of catastrophic landslide dynamics: Science, v. 339, p. 1416–1419, doi:10.1126/science.1232887.

Ellis, M.S., and Freeman, V.L., 1984, Geologic map and cross-sections of the Carbondale 30′ × 60′ quadrangle, west-central Colorado: U.S. Geological Survey Coal Investigations Map C-97-A, scale 1:100,000.

Evans, S.G., Guthrie, R.H., Roberts, N.J., and Bishop, N.F., 2007, The disastrous 17 February 2006 rockslide-debris avalanche on Leyte Island, Philippines: A catastrophic landslide in tropical mountain terrain: Natural Hazards and Earth System Sciences, v. 7, p. 89–101, doi:10.5194/nhess-7-89-2007.

Favreau, P., Mangeney, A., Lucas, A., Crosta, G., and Bouchut, F., 2010, Numerical modeling of landquakes: Geophysical Research Letters, v. 37, L15305, doi:10.1029/2010GL043512.

Fleming, R.W., and Johnson, A.M., 1989, Structures associated with strike-slip faults that bound landslide elements: Engineering Geology, v. 27, p. 39–114, doi:10.1016/0013-7952(89)90031-8.

Fleming, R.W., Baum, R.L., and Giardino, M., 1999, Map and description of the active part of the Slumgullion landslide, Hinsdale County, Colorado: U.S. Geological Survey Miscellaneous Investigation Series Map I-2672, 34 p., 3 sheets, scale 1:1000.

Fogg, J., 2014, Mesa County Deputy Sheriff activity report, June 12, 2014, case number 2014-15096: Grand Junction, Colorado, Mesa County Sheriff's Office.

Fukao, Y., 1995, Single-force representation of earthquakes due to landslides or the collapse of caverns: Geophysical Journal International, v. 122, p. 243–248, doi:10.1111/j.1365-246X.1995.tb03551.x.

George, D.L., and Iverson, R.M., 2014, A depth-averaged debris-flow model that includes the effects of evolving dilatancy: II. Numerical predictions and experimental tests: Proceedings of the Royal Society, ser. A, v. 470, 20130820, doi:10.1098/rspa.2013.0820.

Gesch, D.B., Oimoen, M.J., and Evans, G.A., 2014, Accuracy assessment of the U.S. Geological Survey National Elevation Dataset, and comparison with other large-area elevation datasets—SRTM and ASTER: U.S. Geological Survey Open-File Report 2014-1008, 10 p., doi:10.3133/ofr20141008.

Glicken, H., 1996, Rockslide-debris avalanche of May 18, 1980, Mount St. Helens volcano, Washington: U.S. Geological Survey Open-File Report 96-677, 90 p., 5 plates, http://pubs.usgs.gov/of/1996/0677/.

Guerriero, L., Revelinno, P., Coe, J.A., Focareta, M., Grelle, G., Albanese, V., Corazza, A., and Guadagno, F.M., 2013, Multi-temporal maps of the Montaguto landslide in southern Italy from 1954 to 2010: Journal of Maps, v. 9, p. 135–145, doi:10.1080/17445647.2013.765812.

Guerriero, L., Coe, J.A., Revellino, P., Grelle, G., Pinto, F., and Guadagno, F.M., 2014, Influence of slip-surface geometry on earth-flow deformation, Montaguto earth flow, southern Italy: Geomorphology, v. 219, p. 285–305, doi:10.1016/j.geomorph.2014.04.039.

Handwerger, A.L., Roering, J.J., Schmidt, D.A., and Rempel, A.W., 2015, Kinematics of earthflows in the northern California Coast Ranges using satellite interferometry: Geomorphology, v. 246, p. 321–333, doi:10.1016/j.geomorph.2015.06.003.

Heim, A., 1932, Begrsturz und Menschenleben [English translation by Skermer, N.A, 1989, *in* Landslides and Human Lives, Vancouver, British Columbia, BiTech Publishers]: Zurich, Fretz and Wasmuth Verlag, 218 p.

Helmstetter, A., and Garambois, S., 2010, Seismic monitoring of Sechilienne rockslide (French Alps): Analysis of seismic signals and their correlation with rainfalls: Journal of Geophysical Research, v. 115, F03016, doi:10.1029/2009JF001532.

Herrmann, R.B., 2002, Computer Programs in Seismology: An overview of synthetic seismogram computation, version 3.30: Saint Louis, Missouri, Saint Louis University, Department of Earth and Atmospheric Sciences, 172 p., http://www.eas.slu.edu/eqc/eqc_cps/CPS/CPS330.html.

Herrmann, R.B., Ammon, C.J., and Benz, H., 2013, Group velocity dispersion for North America: http://www.eas.slu.edu/eqc/eqc_research/NATOMO (accessed June 2015).

Hibert, C., Ekstrom, G., and Stark, C.P., 2014, Dynamics of the Bingham Canyon Mine landslides from seismic signal analysis: Geophysical Research Letters, v. 41, p. 4535–4541, doi:10.1002/2014GL060592.

Hsü, K.J., 1975, Catastrophic debris streams (sturzstroms) generated by rockfalls: Geological Society of America Bulletin, v. 86, p. 129–140, doi:10.1130/0016-7606(1975)86<129:CDSSGB>2.0.CO;2.

Huang, C., Yin, H., Chen, C., Yeh, C., and Wang, C., 2007, Ground vibrations produced by rock motions and debris flows: Journal of Geophysical Research, v. 112, F02014, doi:10.1029/2005JF000437.

Huggel, C., Zgraggen-Oswald, S., Haeberli, W., Kaab, A., Polkvoj, A., Galushkin, I., and Evans, S.G., 2005, The 2002 rock/ice avalanche at Kolka/Karmadon, Russian Caucasus: Assessment of extraordinary avalanche formation and mobility, and application of QuickBird satellite imagery: Natural Hazards and Earth System Sciences, v. 5, p. 173–187, doi:10.5194/nhess-5-173-2005.

Hungr, O., 1995, A model for runout analysis of rapid flow slides, debris flows and avalanches: Canadian Geotechnical Journal, v. 32, p. 610–623, doi:10.1139/t95-063.

Hungr, O., 2006, Rock avalanche occurrence, process, and modeling, *in* Evans, S.G., Scarascia Mugnozza, G., Strom, A., and Hermanns, R.L., eds., Landslides from Massive Rock Slope Failure: New Models for Hazard Assessment: NATO Series IV, v. 49, p. 243–266.

Hungr, O., and Evans, S.G., 2004, Entrainment of debris in rock avalanches: An analysis of a long run-out mechanism: Geological Society of America Bulletin, v. 116, p. 1240–1252, doi:10.1130/B25362.1.

Hungr, O., Leroueil, S., and Picarelli, L., 2014, The Varnes classification of landslide types, an update: Landslides, v. 11, p. 167–194, doi:10.1007/s10346-013-0436-y.

Hutchinson, J.N., and Bhandari, R.K., 1971, Undrained loading: A fundamental mechanism of mudflows and other mass movements: Geotechnique, v. 21, p. 353–358, doi:10.1680/geot.1971.21.4.353.

Iverson, R.M., 1997, The physics of debris flows: Reviews of Geophysics, v. 35, p. 245–296, doi:10.1029/97RG00426.

Iverson, R.M., and Denlinger, R.P., 2001, Flow of variably fluidized granular masses across three-dimensional terrain: 1. Coulomb mixture theory: Journal of Geophysical Research, v. 106, p. 537–552, doi:10.1029/2000JB900329.

Iverson, R.M., and George, D.L., 2014, A depth-averaged debris-flow model that includes the effects of evolving dilatancy: I. Physical basis: Proceedings of the Royal Society, ser. A, v. 470, 20130819, doi:10.1098/rspa.2013.0819.

Iverson, R.M., and Ouyang, C., 2015, Entrainment of bed material by earth-surface mass flows: Review and reformulation of depth-integrated theory: Reviews of Geophysics, v. 53, p. 27–58, doi:10.1002/2013RG000447.

Iverson, R.M., and Vallance, J.W., 2001, New views of granular mass flows: Geology, v. 29, p. 115–118, doi:10.1130/0091-7613(2001)029<0115:NVOGMF>2.0.CO;2.

Iverson, R.M., George, D.L., Allstadt, K., Reid, M.R., Collins, B.D., Vallance, J.W., Schilling, S.P., Godt, J.W., Cannon, C.M., Magirl, C.S., Baum, R.L., Coe, J.A., Schulz, W.H., and Bower, J.B., 2015, Landslide mobility and hazards: Implications of the 2014 Oso disaster: Earth and Planetary Science Letters, v. 412, p. 197–208, doi:10.1016/j.epsl.2014.12.020.

Kanamori, H., and Given, J.W., 1982, Analysis of long-period seismic waves excited by the May 18, 1980, eruption of Mount St. Helens—A terrestrial monopole?: Journal of Geophysical Research, v. 87, p. 5422–5432, doi:10.1029/JB087iB07p05422.

Kelfoun, K., and Druitt, T.H., 2005, Numerical modeling of the emplacement of the Scompa rock avalanche, Chile: Journal of Geophysical Research, v. 110, B12202, doi:10.1029/2005JB003758.

Kennett, B.L.N., Engdahl, E.R., and Buland, R., 1995, Constraints on seismic velocities in the Earth from travel times: Geophysical Journal International, v. 122, p. 108–124, doi:10.1111/j.1365-246X.1995.tb03540.x.

Kowalski, J., and McElwaine, J.N., 2013, Shallow two-component gravity-driven flows with vertical variation: Journal of Fluid Mechanics, v. 714, p. 434–462, doi:10.1017/jfm.2012.489.

Kunk, M.J., Budahn, J.R., Unruh, D.M., Stanley, J.O., Kirkham, R.M., Bryant, B., Scott, R.B., Lidke, D.J., and Streufert, R.K., 2002, $^{40}Ar/^{39}Ar$ ages of late Cenozoic volcanic rocks within and around the Carbondale and Eagle collapse centers, Colorado: Constraints on the timing of evaporite-related collapse and incision of the Colorado River, *in* Kirkham, R.M., Scott, R.B.,

and Judkins, T.W., eds., Late Cenozoic Evaporite Tectonism and Volcanism in West-Central Colorado: Geological Society of America Special Paper 366, p. 213–234, doi:10.1130/0-8137-2366-3.213.

Legros, F., 2002, The mobility of long-runout landslides: Engineering Geology, v. 63, p. 301–331, doi:10.1016/S0013-7952(01)00090-4.

McCabe, G.J., Clark, M.P., and Hay, L.E., 2007, Rain-on-snow events in the western United States: Bulletin of the American Meteorological Society, v. 88, p. 319–328, doi:10.1175/BAMS-88-3-319.

McDougall, S., and Hungr, O., 2004, A model for the analysis of rapid landslide motion across three-dimensional terrain: Canadian Geotechnical Journal, v. 41, p. 1084–1097, doi:10.1139/t04-052.

McSaveney, M.J., 1978, Sherman Glacier rock avalanche, Alaska, U.S.A., *in* Voight, B., ed., Rockslides and Avalanches, 1: Natural Phenomena: Amsterdam, Elsevier, Developments in Geotechnical Engineering, v. 14A, p. 197–258.

McSaveney, M., and Davies, T., 2007, Rockslides and their motion, *in* Sassa, K., Fukuoka, H., Wang, F., and Wang, G., eds., Progress in Landslide Science: Berlin, Springer, p. 113–133.

McSaveney, M.J., and Downes, G., 2002, Application of landslide seismology to some New Zealand rock avalanches, *in* Rybar, J., Stemberk, J., and Wagner, P., eds., Landslides: Lisse, Netherlands, Balkema, p. 649–654.

Moretti, L., Mangeney, A., Capdeville, Y., Stutzmann, E., Huggel, C., Schneider, D., and Bouchut, F., 2012, Numerical modeling of the Mount Stellar landslide flow history and of the generated long period seismic waves: Geophysical Research Letters, v. 39, L16402, doi:10.1029/2012GL052511.

Moretti, L., Allstadt, K., Mangeney, A., Capdeville, Y., Stutzmann, E., and Bouchut, E., 2015, Numerical modeling of the Mount Meager landslide constrained by its force history derived from seismic data: Journal of Geophysical Research, v. 120, p. 2579–2599, doi:10.1002/2014JB011426.

Paguican, E.M.B., van Wyk de Vries, B., and Lagmay, A., 2014, Hummocks: How they form and how they evolve in rockslide-debris avalanches: Landslides, v. 11, p. 67–80, doi:10.1007/s10346-012-0368-y.

Parise, M., 2003, Observation of surface features on an active landslide, and implications for understanding its history of movement: Natural Hazards and Earth System Sciences, v. 3, p. 569–580, doi:10.5194/nhess-3-569-2003.

Parise, M., Moscariello, A., and Fleming, R.W., 1997, Evidence from flank ridges for long-term diminishing movement of the Slumgullion landslide, Hinsdale County, Colorado: U.S. Geological Survey Open-File Report 97-517, 14 p.

Perica, S., Martin, D., Pavlobvic, S., Roy, I., St Laurent, M., Trypaluk, C., Unruh, D., Yekta, M., and Bonnin, G., 2013, Precipitation-Frequency Atlas of the United States, Volume 8, Version 2.0: Midwestern States (Colorado, Iowa, Kansas, Michigan, Minnesota, Missouri, Nebraska, North Dakota, Oklahoma, South Dakota, Wisconsin): National Oceanic and Atmospheric Administration Atlas 14, 49 p., 6 appendices.

Pudasaini, S.P., and Hutter, K., 2007, Avalanche Dynamics: Dynamics of Rapid Flows of Dense Granular Avalanches: Netherlands, Springer, 602 p.

Quenouille, M.H., 1956, Notes on bias in estimation: Biometrika, v. 43, p. 353-360.

Rosser, N., Lim, M., Petley, D., Sunning, S., and Allison, R., 2007, Patterns of precursory rockfall prior to slope failure: Journal of Geophysical Research, v. 112, F04014, doi:10.1029/2006JF000642.

Sassa, K., 1985, The mechanism of debris flows, *in* Proceedings of the XI International Conference on Soil Mechanics and Foundation Engineering, San Francisco, California, 12-16 August 1986, v. 3: Rotterdam, Balkema, p. 1173–1176.

Sassa, K., 1988, Geotechnical model for the motion of landslides, *in* Bonnard, C., ed., Landslides: Rotterdarm, Balkema, Proceedings of the 5th International Symposium on Landslides, v. 1, p. 37–56.

Sassa, K., Fukuoka, H., Wang, G.H., and Ishikawa, N., 2004, Undrained dynamic-loading ring shear apparatus and its application to landslide dynamics: Landslides, v. 1, p. 7–19, doi:10.1007/s10346-003-0004-y.

Savage, S.B., 1979, Gravity flow of cohesionless granular materials in chutes and channels: Journal of Fluid Mechanics, v. 92, p. 53–96, doi:10.1017/S0022112079000525.

Savage, S.B., and Hutter, K., 1989, The motion of a finite mass of granular material down a rough incline: Journal of Fluid Mechanics, v. 199, p. 177–215, doi:10.1017/S0022112089000340.

Schneider, D., Bartlet, P., Caplan-Auerbach, J., Christen, M., Huggel, C., and McArdell, B.W., 2010, Insights into rock-ice avalanche dynamics by combined analysis of seismic recordings and a numerical avalanche model: Journal of Geophysical Research, v. 115, F04026, doi:10.1029/2010JF001734.

Schulz, W.H., Harp, E.L., and Jibson, R.W., 2008, Characteristics of large rock avalanches triggered by the November 3, 2002 Denali Fault earthquake, Alaska, USA, *in* Chen, Z., Zhang, J., Li, Z., Wu, F., Ho, K., eds., Landslides and Engineered Slopes, From the Past to the Future: Proceedings of the 10th International Symposium on Landslides, Xi'an, China: London, Taylor & Francis Group, v. 2, p. 1447–1453.

Shea, T., and van Wyk de Vries, B., 2008, Structural analysis and analogue modeling of the kinematics and dynamics of rockslide avalanches: Geosphere, v. 4, p. 657–686, doi:10.1130/GES00131.1.

Soule, J.M., 1988, Surficial-geologic and landslide map of Vega Reservoir and vicinity, Mesa County, Colorado: Colorado Geological Survey Open-File Report 88-1, 2 plates, scale 1:24,000.

Tukey, J.W., 1958, Bias and confidence in not-quite large samples: The Annals of Mathematical Statistics, v. 29, p. 614.

Vanden Berg, M.D., 2008, Basin-wide evaluation of the uppermost Green River Formation's oil-shale resource, Uinta Basin, Utah and Colorado: Utah Geological Survey Special Study 128, 19 p., http://geology.utah.gov/online/ss/ss-128/ss-128txt.pdf.

Voight, B., ed., 1978, Rockslides and Avalanches, 1: Natural Phenomena: Amsterdam, Elsevier, Developments in Geotechnical Engineering, v. 14A, 833 p.

Voight, B., and Sousa, J., 1994, Lessons from Ontake-san—A comparative analysis of debris avalanche dynamics: Engineering Geology, v. 38, p. 261–297, doi:10.1016/0013-7952(94)90042-6.

White, J.L., Morgan, M.L., and Berry, K.A., 2015, The West Salt Creek landslide: A catastrophic rockslide and rock/debris avalanche in Mesa County, Colorado: Colorado Geological Survey Bulletin 55, 45 p., 2 plates.

Xu, Q., Shang, Y., van Asch, T., Wang, S., Zhang, Z., and Dong, X., 2012, Observations from the large, rapid Yigong rock slide–debris avalanche, southeast Tibet: Canadian Geotechnical Journal, v. 49, p. 589–606, doi:10.1139/t2012-021.

Yamada, M., Matsuchi, Y., Chigira, M., and Mori, J., 2012, Seismic recordings of landslides caused by Typhoon Talas (2011), Japan: Geophysical Research Letters, v. 39, L13301, doi:10.1029/2012GL052174.

Yamada, M., Kumagai, H., Matsushi, Y., and Matsuzawa, T., 2013, Dynamic landslide processes revealed by broadband seismic records: Geophysical Research Letters, v. 40, p. 2998–3002, doi:10.1002/grl.50437.

Yeend, W.E., 1969, Quaternary geology of the Grand and Battlement Mesa area, Colorado: U.S. Geological Survey Professional Paper 617, 50 p., 1 plate, scale 1:96,000.

Yeend, W.E., 1973, Slow-sliding slumps, Grand Mesa, Colorado: The Mountain Geologist, v. 10, p. 25–28.

Zanchetta, G.R., Sulpizio, R., Pareschi, M.T., Leoni, F.M., and Santacroce, R., 2004, Characteristics of May 5–6, 1998 volcaniclastic debris flows in the Sarno area (Campania, southern Italy): Relationships to structural damage and hazards zonation: Journal of Volcanology and Geothermal Research, v. 133, p. 377–393, doi:10.1016/S0377-0273(03)00409-8.